

HUMBOLDT-UNIVERSITÄT ZU BERLIN  
MATHEMATISCH-NATURWISSENSCHAFTLICHE FAKULTÄT  
INSTITUT FÜR PHYSIK

## **MoS<sub>2</sub> on gold substrate**

Masterarbeit

zur Erlangung des akademischen Grades  
Master of Science (M. Sc.)

eingereicht von: Juliane Mörsel

geboren am: 18.06.1989

geboren in: Gera

Gutachter/innen: Prof. Claudia Draxl  
PD Dr. Pasquale Pavone

Betreuer: Dr. Ronaldo Rodrigues Pela

eingereicht am: ..... verteidigt am: .....



To my father and grandfather,  
in loving memory.



## Abstract

In this work, we perform ab-initio calculations with the full-potential all-electron package **exciting** to investigate the impact of Au(111) substrate on the optoelectronic properties of MoS<sub>2</sub>. The electronic properties are obtained, using both density-functional theory and the  $G_0W_0$  approximation. To study optical transitions in the heterostructure, Bethe-Salpeter equation within the  $GW$  approach is employed. We show how the electronic bandgap of MoS<sub>2</sub>. in the MoS<sub>2</sub> on a gold heterostructure as well as the exciton binding energy are decreased.



---

# Contents

<b>1</b>	<b>Introduction</b>	<b>1</b>
<b>2</b>	<b>Theoretical background</b>	<b>3</b>
2.1	The many-body problem of a solid . . . . .	3
2.1.1	Density-functional theory . . . . .	4
2.1.2	Kohn-sham equations . . . . .	5
2.2	Beyond DFT: Many-body perturbation theory . . . . .	6
2.2.1	$GW$ approximation for the self energy . . . . .	6
2.2.2	One-shot approximation: $G_0W_0$ . . . . .	7
2.2.3	Bethe-Salpeter Equation . . . . .	8
<b>3</b>	<b>Computational method and parameters</b>	<b>11</b>
3.1	The software package <code>exciting</code> . . . . .	11
3.1.1	Augmented plane waves . . . . .	11
3.1.2	LAPW+lo basis set . . . . .	12
3.1.3	Solution of the KS-equations . . . . .	12
3.2	Computational details . . . . .	13
<b>4</b>	<b>Structure of <math>\text{MoS}_2@Au(111)</math></b>	<b>15</b>
4.1	Crystal parameter of $\text{MoS}_2$ monolayer . . . . .	15
4.2	Crystal parameter of bulk $Au(111)$ . . . . .	16
4.3	Building the $\text{MoS}_2@Au(111)$ compound . . . . .	17
4.3.1	Supercell . . . . .	17
4.3.2	$\text{MoS}_2$ unit cell matched on $Au(111)$ . . . . .	18
<b>5</b>	<b>Results</b>	<b>21</b>
5.1	Structural parameters . . . . .	21
5.2	Electronic structure . . . . .	22
5.2.1	Kohn-sham band structure and pDOS . . . . .	22
5.2.2	Charge density distribution . . . . .	29
5.2.3	Electronic properties from $G_0W_0$ . . . . .	32
5.3	Optical properties . . . . .	34
5.3.1	Dielectric function . . . . .	34
5.3.2	Exciton wave function . . . . .	37
<b>6</b>	<b>Conclusions and outlook</b>	<b>41</b>

<b>A Effect of biaxial strain on the MoS<sub>2</sub> band gap</b>	<b>45</b>
<b>B Species files</b>	<b>47</b>
<b>References</b>	<b>55</b>

---

## Introduction

Since the manufacturing of graphene in 2004 [1], two-dimensional materials have been of high interest in condensed matter physics and materials science [2]. Among these materials, particular attention has been given to transition metal dichalcogenides (TMDs). Their chemical formula is  $\text{MX}_2$ , with the transition metal M (*e.g.*, Mo or W) sandwiched by two dichalcogenides atoms X (*e.g.*, S, Se, or Te). TMDs are promising materials for optoelectronic applications and devices, *e.g.*, field-effect transistors [3, 4] and photovoltaics [5]. As a further benefit of these materials, they are easily synthesized by liquid exfoliation [6], or chemical vapor deposition [7]. In this work, we focus on monolayer  $\text{MoS}_2$ .

$\text{MoS}_2$  is a semiconductor with a direct band gap in the monolayer structure [8]. The crystal structure of  $\text{MoS}_2$  consists of two hexagonal-shaped layers of sulfur atoms with an intermediate layer of molybdenum [9]. The bonding between Mo and S atoms is covalent, whereas, in bulk material,  $\text{MoS}_2$  sheets are bonded by van der Waals interaction and, therefore, easily separated. Moreover, monolayer  $\text{MoS}_2$  has a reduced dielectric screening, strongly bound excitons, and intense charge-carrier interaction due to the quantum confinement in the out-of-plane direction. These properties place  $\text{MoS}_2$  among the most interesting candidates for the next generation of optoelectronic devices. However, these properties are sensitive to the dielectric environment and differ for isolated  $\text{MoS}_2$  and  $\text{MoS}_2$  deposited on a substrate. Consequently, it is crucial to understand the impact of a substrate on the band structure and excitonic effects. In particular, metallic substrates are interesting because many applications and devices use metallic contacts. In this work, we investigate the impact of a gold substrate.

In experiments, the placement of  $\text{MoS}_2$  on gold shows a Moiré pattern due to the lattice mismatch of both materials [10]. In this work, we analyze the  $\text{MoS}_2@Au(111)$  structure in a supercell configuration as shown in Figure 1.1. Furthermore, we explore an alternative approach with matched unit cells of both materials to mimic the different stacking sequences of the Moiré pattern.

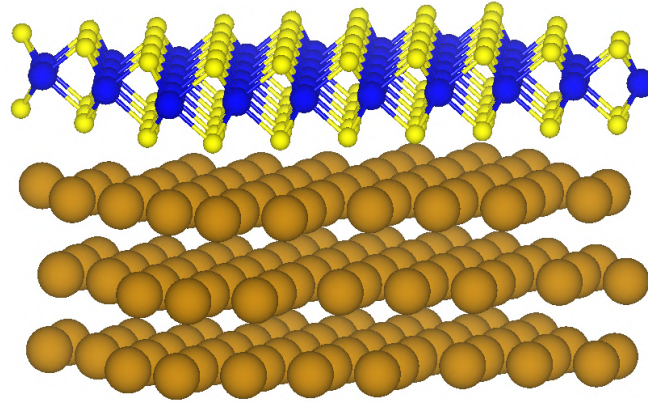


**Figure 1.1:** Supercell MoS<sub>2</sub> on gold.

The aim of this work is the theoretical first-principles determination of the electronic band gap, optical transitions, and exciton binding energy of MoS<sub>2</sub> on top of the gold substrate. All calculations are carried out with the all-electron full-potential package `exciting` [11], implementing the linearized augmented plane-wave method with local orbitals (LAPW+lo). We used density functional theory for the electronic properties, *i.e.*, band structure and density of states. Additionally,  $G_0W_0$  approximation is employed as the state-of-the-art methodology to obtain electronic features. Optical transitions are investigated with the Bethe-Salpeter equation within the  $GW$  approach.

In the first chapter, we briefly introduce the theoretical background. We continue with the presentation of the used software package, its concept, and implemented workflow. This section ends with the presentation of the used computational parameter. Further on, we describe the different employed configurations of MoS<sub>2</sub>@Au(111). In the last chapter, we present our results for the electronic and optical properties of pristine MoS<sub>2</sub> and MoS<sub>2</sub>@Au(111) in a selected geometry.

---

## Theoretical background

In this chapter, we give the basic physical theory to describe the electronic and optical properties of a solid. We start with the description of the many-body problem and introduce the common theory to approach its ground-state properties: Density-functional theory (DFT). Further on, the *GW* approximation, a many-body perturbation theory beyond DFT is introduced. The *GW* approximation is the state-of-the-art approach to compute the electronic band structure. In the last section of this chapter, the Bethe-Salpeter equation, an approach to calculate the absorption spectra and excitonic effects, is presented.

### 2.1 The many-body problem of a solid

The full quantum-mechanical description of a solid system, contained in its wave function, can be obtained by solving the corresponding many-body Schrödinger equation. However, for an extended system this equation cannot be solved directly due to the infinite degrees of freedom. In order to reduce the complexity of the problem one usually assumes the Born-Oppenheimer approximation (BOA) [12], which decouples the electronic and nuclear behaviour. By fixing the position of the nuclei to a given configuration one obtains an effective Schrödinger equation for the electrons that reads:

$$\hat{H}_e \varphi(r; R) = [\hat{T} + \hat{W} + \hat{V}_{ext}(R)] \varphi(r; R) = E(R) \varphi(r; R) \quad (2.1)$$

where  $\varphi(r; R)$  is the electronic wave function,  $\hat{T}$  is the kinetic energy operator of the electrons,  $\hat{W}$  is the interaction operator between the electrons,  $\hat{V}_{ext}(R)$  is the external potential of the nuclei, and  $E(R)$  is the total electronic energy of the system. The electronic positions are described by the vector  $r = \{\mathbf{r}_i; i = 1 \dots N\}$ , and the fixed positions of the nuclei by  $R = \{\mathbf{R}_I; I = 1 \dots N_n\}$ .

Although the electronic and nuclear systems are decoupled, it is still a huge many-body system when considering electrons in solids. There are different approaches to solve the electronic Schrödinger equation. In this work, we use density-functional

theory (DFT). The benefit of this approach is the usage of the density  $n(\mathbf{r})$  as main descriptor instead of the wave function  $\varphi(\mathbf{r}_1, \dots, \mathbf{r}_N)$ , reducing the degree of freedom from  $3N$  to 3.

### 2.1.1 Density-functional theory

The validity of DFT is based on the Hohenberg-Kohn (HK) theorems [13]. The first HK theorem states that the external potential  $\hat{V}_{ext}$  defined by

$$\hat{V}_{ext} = \sum_{i=1}^N v_{ext}(\mathbf{r}_i) \quad (2.2)$$

has a one-to-one correspondence with the ground-state electron density. With the external potential we can determine all states of the quantum system including the ground state as well as all excited states. Therefore, we can write the total ground-state energy as functional of the (ground-state) electron density  $n(\mathbf{r})$ .

$$E_{GS}[n] = \int v_{ext}(\mathbf{r}) n(\mathbf{r}) d\mathbf{r} + F[n]. \quad (2.3)$$

Here,  $F[n]$  is the Hohenberg-Kohn functional and includes the kinetic and interaction energy of the electrons.

The ground-state total-energy functional can be minimized with respect to the density:

$$E_{GS}[n_{GS}] = \min_{n(\mathbf{r})} E_{GS}[n] \quad (2.4)$$

After minimization, the minimizing electron density  $n$  is the exact ground-state density  $n_{GS}$  and the corresponding energy is the ground-state energy  $E_{GS}[n_{GS}]$ . Starting from the total energy functional Eq.(2.3) Kohn and Sham divided the Hohenberg-Kohn functional  $F[n]$  in three parts:

$$F[n] = E_H[n] + T_0[n] + E_{xc}[n]. \quad (2.5)$$

The first term in Eq.(2.3) is the Hartree energy functional and takes the classical electrostatic interaction into account:

$$E_H[n] = \frac{1}{2} \int \int \frac{n(\mathbf{r}) n(\mathbf{r}')}{|\mathbf{r} - \mathbf{r}'|} d\mathbf{r} d\mathbf{r}'. \quad (2.6)$$

$T_0[n]$  is the kinetic energy of non-interacting electrons.  $E_{xc}[n]$  is by definition the exchange-correlation energy of the system. It includes all many-body interactions which are not included in the other functionals. Following the Hohenberg-Kohn theorem,

the constrained minimization of the total energy with respect to the electron density  $n(\mathbf{r})$  can be performed with the help of the lagrangian multiplier  $\mu$

$$\frac{\delta(E - \mu N)}{\delta n} = \frac{\delta T_0[n(\mathbf{r})]}{\delta n(\mathbf{r})} + \int \frac{n(\mathbf{r}')}{|\mathbf{r} - \mathbf{r}'|} d\mathbf{r}' + v_{xc}(\mathbf{r}, [n]) + v_{ext}(\mathbf{r}) - \mu = 0 \quad (2.7)$$

with the exchange-correlation potential defined as

$$v_{xc}(\mathbf{r}, [n]) = \frac{\delta E_{xc}[n(\mathbf{r})]}{\delta n(\mathbf{r})} \quad (2.8)$$

The lagrangian multiplier  $\mu$  takes the constraint  $N = \int n(\mathbf{r}) d\mathbf{r}$  into account.

### 2.1.2 Kohn-sham equations

The minimization problem described by Eq. (2.7) can be solved using a auxiliary non-interacting system (the KS system) which has the exact electron density given as the sum of the contributions of non-interacting single-particle wave functions  $\{\chi_i(\mathbf{r})\}$

$$n_{GS}(\mathbf{r}) = \sum_i^N |\chi_i(\mathbf{r})|^2. \quad (2.9)$$

The  $\{\chi_i(\mathbf{r})\}$  satisfy the Kohn-Sham (KS) equations [14]:

$$h_{KS} \chi_i(\mathbf{r}) \equiv \left\{ -\frac{1}{2} \nabla^2 + v_{KS}(\mathbf{r}, [n]) \right\} \chi_i(\mathbf{r}) = \varepsilon_i \chi_i(\mathbf{r}) \quad i = 1, \dots, N \quad (2.10)$$

with the KS potential defined as

$$v_{KS}(\mathbf{r}, [n]) = v_{ext}(\mathbf{r}) + \int \frac{n(\mathbf{r}')}{|\mathbf{r} - \mathbf{r}'|} d\mathbf{r}' + v_{xc}(\mathbf{r}, [n]). \quad (2.11)$$

The KS potential depends on the electron density. Hence, the KS equations must be solved in a self-consistent cycle shown in Figure 2.1. Starting point is an arbitrary density to calculate the KS potential. With the energies and wave functions from this potential, a density can be calculated. If the new density is equal to the density one step before the wanted density is found, otherwise the self-consistent cycle is repeated.

The solution of the Kohn-Sham equations leads to the exact  $n_{GS}$ . However, the exact expression for the exchange-correlation term  $E_{xc}[n]$  is not known. Hence, we need to approximate this functional. The first level of approximation is the local-density approximation (LDA). LDA is derived from the solutions of the homogeneous electron gas and therefore depends only on the density  $n(\mathbf{r})$ . A more elevated approach is the generalized gradient approximation (GGA) [16, 17] which involves both, the density

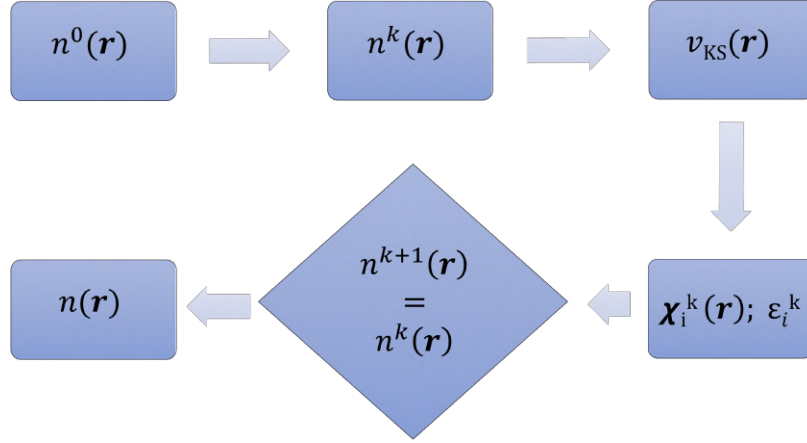


**Figure 2.1:** Schematic representation of the self-consistent cycle (adapted from Ref. [15])

$n(\mathbf{r})$  and its gradient:

$$E_{xc}^{GGA} = \int f(n(\mathbf{r}), \nabla n(\mathbf{r})) d\mathbf{r}. \quad (2.12)$$

Further approximations with different accuracy and computational costs were developed and are presented in Ref. [18]. In this work, we used GGA in the PBE flavor [19].

## 2.2 Beyond DFT: Many-body perturbation theory

The Kohn-Sham single-particle energies  $\varepsilon_i$  defined in Eq.(2.10) have no physical meaning. To calculate the actual single-(quasi)particle energies in a solid we have to use an approach beyond DFT. Here, we give an introduction for the  $GW$  and  $G_0W_0$  approximations. Furthermore, the opto-electronic response in  $\text{MoS}_2$  is dominated by strongly-bound electron-hole pairs, which can be considered as quasi particles and are called excitons [20]. To address these effects, we use the two-particle approach related to the Bethe-Salpeter equation (BSE).

### 2.2.1 $GW$ approximation for the self energy

In this section, we discuss a predictive theory beyond the KS-DFT to calculate excitation energies in semiconductors and insulators. One main problem in the KS approach is the calculation of the correct band gap. Although the approximations for the exchange-correlation function in DFT improve towards the exact functional, we still have to face an underestimation of the KS band gap due to the intrinsic “independent-electro” nature of the KS equations. Further, from now on the electrons will be described as quasi particles (QP) including the screening by surrounding electrons into account. The theoretical basis of the  $GW$  approximation is given by the many-body perturbation

theory. The approximation is derived starting from the equation of motion from the one-body Green's function (GF)  $G$ . The GF satisfies a Dyson-like equation with a self-energy kernel

$$G = G_0 + G_0 \Sigma G, \quad (2.13)$$

where  $G_0$  is the GF of a reference non-interacting electron system and  $\Sigma$  the self energy. Further approximations lead to the  $GW$  approximation for the self-energy [21]

$$\Sigma = iGW, \quad (2.14)$$

with the screened coulomb interaction  $W$ . The quasi-particle energies  $\varepsilon_i^{QP}$  and wave functions can be obtained by solving the equation

$$\left( -\frac{1}{2}\nabla^2 + v_{ext} + v_H \right) \psi_i(\mathbf{r}) + \int d\mathbf{r}' \Sigma(\mathbf{r}, \mathbf{r}'; \varepsilon_i^{QP}) \psi_i(\mathbf{r}') = \varepsilon_{n\mathbf{k}}^{QP} \psi_i(\mathbf{r}). \quad (2.15)$$

The first part of Eq.(2.13) again contains the external potential, the single-particle kinetic energy operator and the Hartree term. The self-energy kernel includes all the interaction *i.e.*, the exchange and correlation between the quasi particles.

### 2.2.2 One-shot approximation: $G_0 W_0$

A one-shot (not self-consistent) approximation for the self-energy  $\Sigma$  in Eq.(2.14) is the  $G_0 W_0$  approximation. By adding the exchange-correlation potential from the KS equations to Eq.(2.15), one obtains an expression of the quasi particle energies which reads:

$$\varepsilon_{n\mathbf{k}}^{QP} = \varepsilon_{n\mathbf{k}}^{KS} + Z_{n\mathbf{k}} \left[ \text{Re} \Sigma_{n\mathbf{k}}(\varepsilon_{n\mathbf{k}}^{KS}) - v_{n\mathbf{k}}^{xc} \right], \quad (2.16)$$

where we explicitly introduce the quantum numbers for periodic systems  $i = (n, \mathbf{k})$ ,  $\varepsilon_{n\mathbf{k}}^{KS}$  are the Kohn-Sham energies,  $\Sigma_{n\mathbf{k}}$  and  $v_{n\mathbf{k}}^{xc}$  are the diagonal matrix elements of the (one-shot) self-energy and the exchange-correlation potential [22].  $Z_{n\mathbf{k}}$  is a renormalization factor [22]. The explicit form of the self-energy used in the one-shot  $G_0 W_0$  is given by

$$\Sigma_{xc}(\mathbf{r}, \mathbf{r}'; \omega) = \frac{i}{2\pi} \int G_0(\mathbf{r}, \mathbf{r}'; \omega + \omega') W_0(\mathbf{r}, \mathbf{r}'; \omega') e^{i\omega'\eta} d\omega', \quad (2.17)$$

where  $G_0$  is the non-interacting one-particle Green's function

$$G_0(\mathbf{r}, \mathbf{r}'; \omega) = \sum_{n\mathbf{k}} \frac{\chi_{n\mathbf{k}}(\mathbf{r}) \chi_{n\mathbf{k}}(\mathbf{r}')}{\omega - \varepsilon_{n\mathbf{k}}^{KS}}, \quad (2.18)$$

with the KS single-particle wave functions  $\chi_{n\mathbf{k}}(r)$  and the single-particle energies  $\varepsilon_{n\mathbf{k}}^{KS}$ .  $W_0$  is the screened Coulomb potential

$$W_0(\mathbf{r}, \mathbf{r}'; \omega) = \int \epsilon_{KS}^{-1}(\mathbf{r}, \mathbf{r}''; \omega) v_C(\mathbf{r}'', \mathbf{r}') d\mathbf{r}'' . \quad (2.19)$$

where  $\epsilon_{KS}^{-1}(\mathbf{r}, \mathbf{r}''; \omega)$  is the inverse KS dielectric function and  $v_C$  is the bare coulomb potential.

### 2.2.3 Bethe-Salpeter Equation

With  $GW$  we get the single-particle excitation energies. However, in order to characterize neutral excitations, e.g., optical absorption, we use the Bethe-Salpeter equation (BSE) for the two-particle correlation function  $L$ , given by the Dyson-like equation [23, 24]

$$L = L_0 + L_0 \Xi L, \quad (2.20)$$

where  $\Xi$  is the interaction kernel of the BSE. The solution of Eq.(2.20) leads to an eigenvalue problem with the effective two-particle Hamiltonian [25]

$$H^{\text{eff}} \mathbf{A}^\lambda = E^\lambda \mathbf{A}^\lambda, \quad (2.21)$$

where the effective Hamiltonian in Tamm-Dancoff approximation [26] is defined as

$$H^{\text{eff}} = H^{\text{diag}} + 2\gamma_x H^{\mathbf{x}} + \gamma_c H^{\mathbf{c}}. \quad (2.22)$$

The eigenvalues  $E^\lambda$  and eigenvectors  $A_\alpha^\lambda$  in Eq.(2.21) can be used to express the two-particle correlation function written as

$$L_{\alpha\beta} = i \sum_{\gamma} \frac{A_\alpha^\lambda [A_\beta^\lambda]^*}{\omega - E^\lambda}. \quad (2.23)$$

Analyzing the different contributions to the effective hamiltonian in Eq.(2.22),  $H^{\text{diag}}$  describes the independent-particle transitions.  $H^{\mathbf{x}}$  includes the exchange interaction between the electron and the hole. Therefore, it contains the repulsive interaction with the bare coulomb potential  $v_C(\mathbf{r}, \mathbf{r}')$ . The correlation between particles is taken into account by the last term  $H^{\mathbf{c}}$  with the screened potential  $W(\mathbf{r}, \mathbf{r}')$  which is analogue to Eq.(2.19). By choosing  $\gamma_x$  and  $\gamma_c$  the (spin) level of approximation is defined. When both parameter set to zero a non-interacting system is considered. Further, when both are set equal to one the full Hamiltonian is considered. This channel considers spin-singlets. Otherwise, when  $\gamma_c$  is set to one and  $\gamma_x$  is equal zero, the exchange part is neglected. This channel is called spin-triplet. From the solution the imaginary part

of the macroscopic dielectric function  $\epsilon_M^j(\omega)$  can be obtained as

$$\text{Im } \epsilon_M^j(\omega) = \frac{8\pi^2}{\Omega} \sum_{\lambda} \left| \sum_{\nu c\mathbf{k}} A_{\nu c\mathbf{k}}^{\lambda} \frac{\langle \nu\mathbf{k} | \hat{p}_j | c\mathbf{k} \rangle}{(\epsilon_{c\mathbf{k}} - \epsilon_{\nu\mathbf{k}})} \right|^2 \delta(\omega - E_{\lambda}). \quad (2.24)$$

The polarization is marked with the index  $j$  and  $\Omega$  is the crystal volume.



# 3

---

## Computational method and parameters

Here, we give a short description of the computational implementation of DFT in the software package `exciting`. We start with the introduction of the (linearized) augmented plane-wave method, followed by the solution of the KS equations like it is implemented in `exciting`. In the second part of this chapter, we give the computational parameters used for executing the calculations.

### 3.1 The software package `exciting`

In this section, we introduce the all-electron full-potential software package `exciting` [11], implementing linearized augmented plane-wave methods with local orbitals (LAPW+lo). We give a brief insight in the workflow of the code and point out how the specific implementation is different from other DFT codes.

#### 3.1.1 Augmented plane waves

To solve the KS equations numerically, the single-particle wave functions  $\chi_{n\mathbf{k}}(\mathbf{r})$  are expanded as a linear combination of APW  $\phi_{\mathbf{G}+\mathbf{k}}(\mathbf{r})$ . In order to define the augmented plane waves (APW) the space is divided in the muffin-tin (MT) spheres centered on the atoms, and the interstitial (I) space in between. The MTs have the radii\*  $R_{MT}$  and do not overlap. The linear combination of APW  $\phi_{\mathbf{G}+\mathbf{k}}(\mathbf{r})$  are given with:

$$\chi_{n\mathbf{k}}(\mathbf{r}) = \sum_{\mathbf{G}} C_{\mathbf{G}}^{n\mathbf{k}} \phi_{\mathbf{G}+\mathbf{k}}(\mathbf{r}) \quad (3.1)$$

---

\*The muffin-tin radii may differ for different elements.

where the augmented plane waves are given by

$$\phi_{\mathbf{G}+\mathbf{k}}(\mathbf{r}) = \begin{cases} \sum_{lm} A_{lm}^{\mathbf{G}+\mathbf{k}} u_l(r_\alpha; \varepsilon_l) Y_{lm}(\hat{\mathbf{r}}_\alpha) & r_\alpha \geq R_{MT} \\ \frac{1}{\sqrt{\Omega}} e^{i(\mathbf{G}+\mathbf{k})\mathbf{r}} & \mathbf{r} \in I \end{cases} \quad (3.2)$$

for the MT and the interstitial space. The wave functions of the MTs are expanded with spherical harmonics and radial functions  $u_l$  based on  $r_\alpha = |\mathbf{r} - \mathbf{R}_\alpha|$ , where  $\mathbf{R}_\alpha$  is the position of the atoms. The coefficients  $A_{lm}^{\mathbf{G}+\mathbf{k}}$  ensure that the plane waves are continuous at the sphere boundaries. The radial functions depending on the energy  $\varepsilon$  of the system. However, the APW method leads to a non linear eigenvalue problem, which is very difficult to solve.

### 3.1.2 LAPW+lo basis set

In order to overcome this problem, as an alternative to the APW method, linearized augmented plane waves (LAPW) can be used for the expansion of the basis functions in the MT parts:

$$\phi_{\mathbf{G}+\mathbf{k}}(\mathbf{r}) = \sum_{lm\alpha} \left[ A_{lm\alpha}^{\mathbf{G}+\mathbf{k}} u_l(r_\alpha; \varepsilon_l) + B_{lm\alpha}^{\mathbf{G}+\mathbf{k}} u'_l(r_\alpha; \varepsilon_l) \right] Y_{lm}(\hat{\mathbf{r}}_\alpha) \quad (3.3)$$

where  $u'_l(r; \varepsilon_l)$  is the derivative of the radial functions with respect to the energy and the coefficient  $B_{lm\alpha}^{\mathbf{G}+\mathbf{k}}$  enables the derivatives of the plane waves to be continuous at the MT borders, too. Another method for the linearization is to use local orbitals added to the APWs [27]. The local orbitals are defined such that they are zero in the interstitial space. In the MT-space the local orbitals are defined as:

$$\phi_\nu(\mathbf{r}_\alpha) = [a_\nu u_l(r_\alpha; \varepsilon_l) + b_\nu u'_l(r_\alpha; \varepsilon_l)] Y_{lm}(\hat{\mathbf{r}}_\alpha) \quad (3.4)$$

The coefficients  $a_\nu$  and  $b_\nu$  ensure that the plane waves are normalized and become zero at the MT borders. In the software package `exciting` the local orbitals are implemented in addition to the linearized augmented plane waves method.

### 3.1.3 Solution of the KS-equations

Using the LAPW+lo as basis set, the KS equations can be written as a generalized eigenvalue problem:

$$H^k C^k = \varepsilon^k S^k C^k \quad (3.5)$$

where  $C^k$  are the coefficients defined in Eq.(3.1) and  $H^k$  is the hamiltonian and  $S^k$  the overlap matrix defined by

$$H_{\mathbf{G}\mathbf{G}'}^k = \langle \phi_{\mathbf{G}+\mathbf{k}} | \hat{h}_{ks} | \phi_{\mathbf{G}'+\mathbf{k}} \rangle \quad (3.6)$$

$$S_{\mathbf{G}\mathbf{G}'}^k = \langle \phi_{\mathbf{G}+\mathbf{k}} | \phi_{\mathbf{G}'+\mathbf{k}} \rangle \quad (3.7)$$

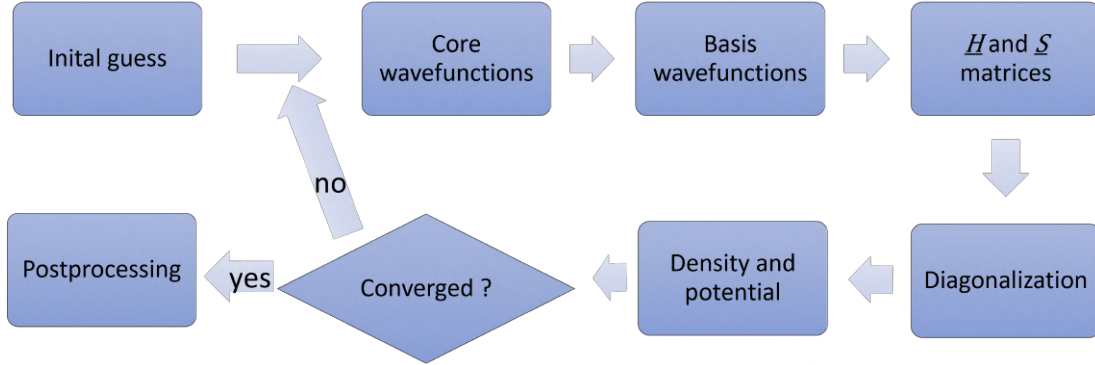


**Figure 3.1:** Schematic representation of the `exciting` workflow (adapted from Ref. [11])

Figure 3.1 shows a flowchart of the `exciting` workflow for a ground-state calculation. Starting point is an initial guess for the density. In the second step, `exciting` calculates the core and basis wave functions. Further on, the hamiltonian and overlap matrices, defined in Eqs. (3.6,3.7) can be evaluated and a new density is obtained. If the convergence criteria are reached, the calculation is finished. Otherwise it starts again using the previously calculated densities.

## 3.2 Computational details

With the aim of studying first the substrate effects on the ground-state properties of MoS<sub>2</sub> isolated monolayer and on gold substrate, we employed the method and software described in the last section using computational parameters presented here.

We specify the basis functions for the MT sphere as described in section 3.1.1. We treat the 1s<sup>2</sup> up to 4d<sup>2</sup> states of Au as core states. For Mo and S we need less states. For Mo we treat all states up to the 3d<sup>2</sup> state as core states. In case of the S atoms, the 1s<sup>2</sup> and 2s<sup>2</sup> state are treated as core states. The actual species files including the used local orbitals for the element Au, Mo, and S are shown in Appendix A.

The structural properties of pristine MoS<sub>2</sub> are obtained through relaxation of the relative positions of the atoms. These relaxations are performed with a 12×12×1

**k**-point mesh. The maximum force on the atoms are set to  $5 \text{ meV \AA}^{-1}$ . The pristine structure are calculated with a  $21 \times 21 \times 1$  **k**-grid mesh. For the three matched geometries the **k**-grid mesh is set to  $20 \times 20 \times 1$ . The supercell with  $(\sqrt{13} \times \sqrt{13})$  unit cells of  $\text{MoS}_2$  on  $(4 \times 4)$   $\text{Au}(111)$  unit cells is calculated with a  $12 \times 12 \times 1$  **k**-grid mesh. The convergence for the basis set size require to set the  $R_{\text{MT}}^{\text{min}} G_{\text{max}}$  value parameter to 8. The ground-state energy threshold is set to 0.3 meV in all calculations. To prevent the  $\text{MoS}_2$  from interaction with its replica, the lattice constant in z-direction is set to 8 times the pristine lattice constant, resulting in a vacuum of about 23 Å. For the matched structures of  $\text{MoS}_2$  on  $\text{Au}(111)$  expansion of the constant in z-direction is 10 times the pristine lattice constant, giving a vacuum size of about 20 Å. The mismatched structure has a vacuum size of about 12 Å. The muffin-tin radii values are 2.40, 2.05, and 2.60 bohr for Mo, S, and Au, respectively. Furthermore, we used the Pulay mixing method with the Kerker preconditioner [28] as implemented in `exciting` for the ground state calculations.

The  $G_0W_0$  calculations are performed with 100 empty states and a  $18 \times 18 \times 1$  **k**-grid mesh for pristine  $\text{MoS}_2$  and  $\text{MoS}_2/\text{Au}$  system in hcp geometry. The DFT calculation beforehand is repeated with a  $21 \times 21 \times 1$  **k**-grid mesh for freestanding  $\text{MoS}_2$  and  $\text{MoS}_2/\text{Au}$ . The vacuum size for the hcp-structure is 14 Å. A cut-off for the Coulomb potential in z-direction is employed. To enhance the accuracy of  $G_0W_0$  calculations, a increased number of local orbitals is advised [29]. The used local orbitals for Au, Mo, and S are integrated in the species files.

BSE computations are performed within the Tamm-Dancoff approximation [26]. For the correction of the fundamental gap of pristine  $\text{MoS}_2$  we employ a scissor operator with 1.22 eV to mimic the quasi-particle band gap calculated with  $GW$ . For the metallic compound system  $\text{MoS}_2/\text{Au}(111)$  no scissor operator is employed. Instead, the BSE calculation is executed ontop of  $GW$ . The **k**-grid mesh is set to  $18 \times 18 \times 1$  for both the pristine and junction materials. For Au a  $6 \times 6 \times 1$  **k**-point mesh is applied. The number of empty states is set to 100 for pristine  $\text{MoS}_2$ . 5 valence band and 5 conduction band are included for evaluating the transitions. In the case of the  $\text{MoS}_2/\text{Au}(111)$  junction, the band range is set consistent with the contributing bands of Mo and S to match the expected band gap of  $\text{MoS}_2$ . The Lorentzian broadening is set to 0.108 eV for all calculations. To remove contributions of the vacuum in the dielectric function of the slab materials, we replace the crystal volume  $\Omega$  in Eq. (??) with an effective volume  $\Omega_{\text{slab}}$  of the slab material as derived in [30]

$$\Omega_{\text{slab}} = \frac{d_{\text{eff}}}{c} \Omega \quad (3.8)$$

where  $c$  is the length of the lattice parameter in z-direction and  $d_{\text{eff}}$  is the effective thickness of the slab.

---

## Structure of MoS<sub>2</sub>@Au(111)

In this chapter, we present how the MoS<sub>2</sub> on Au compound is implemented. Therefore, we compare the crystal structure of both materials. We will show the size difference between the crystal lattices of both unit cells. We present a potential supercell. Since a supercell requires quite more atoms, the heterostructure becomes computationally expensive. Therefore, we generate adapted matched unit cells to overcome the computational costs and, nevertheless, get insight in (opto-)electronic properties of MoS<sub>2</sub> on gold substrate.

### 4.1 Crystal parameter of MoS<sub>2</sub> monolayer

In this section we discuss how a structure from MoS<sub>2</sub> on a gold substrate can be obtained. First we compare the lattice constants of both materials, starting with the monolayer MoS<sub>2</sub>. As can be seen in Figure 4.1 MoS<sub>2</sub> has a honeycomb structure with one molybdenum atom (blue) sandwiched by two chalcogenide atoms (yellow) in the primitive unit cell. The experimental lattice constant of MoS<sub>2</sub> is  $a = 3.15 \text{ \AA}$  [31].

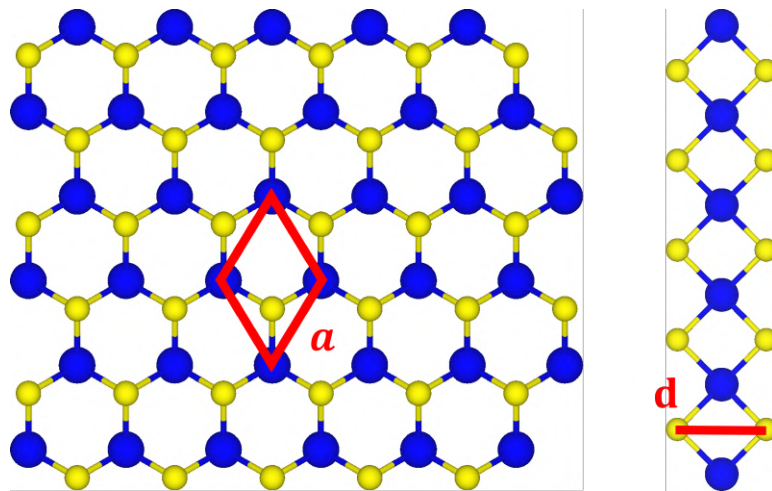


**Figure 4.1:** Top view (left) and side view (right) of MoS<sub>2</sub>. The primitive unit cell (red) with lattice constant  $a$  and the thickness  $d$ .

## 4.2 Crystal parameter of bulk Au(111)

As a substrate we chose gold Figure 4.2. Gold is a metal with a face-centered crystal structure. The primitive unit cell contains four atoms and has a lattice constant  $a_{\text{Au, primitive}} = 4.07 \text{ \AA}$  [32]. As a surface the (111)-direction was chosen, coloured violet in Figure 4.2. In the following the gold substrate will be labeled Au(111).

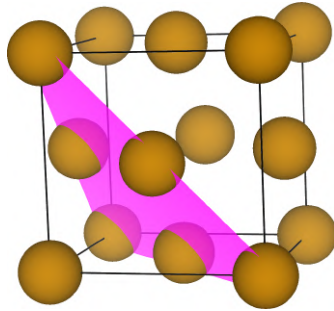


**Figure 4.2:** Face-centered unit cell of gold with (111)-plane (violet).

To match the monolayer MoS<sub>2</sub> on Au(111) we construct a unit cell such that the (111)-direction is parallel to the out-of-plane direction of MoS<sub>2</sub>. The new unit cell of gold has a rhombus shape in top view as can be seen in Figure 4.3. The new unit cell contains three atoms. The adapted lattice constant is  $a'_{\text{Au}} = 2.88 \text{ \AA}$ . In (111)-direction the unit cell has now the lattice vector  $c'_{\text{Au}} = 7.05 \text{ \AA}$ .

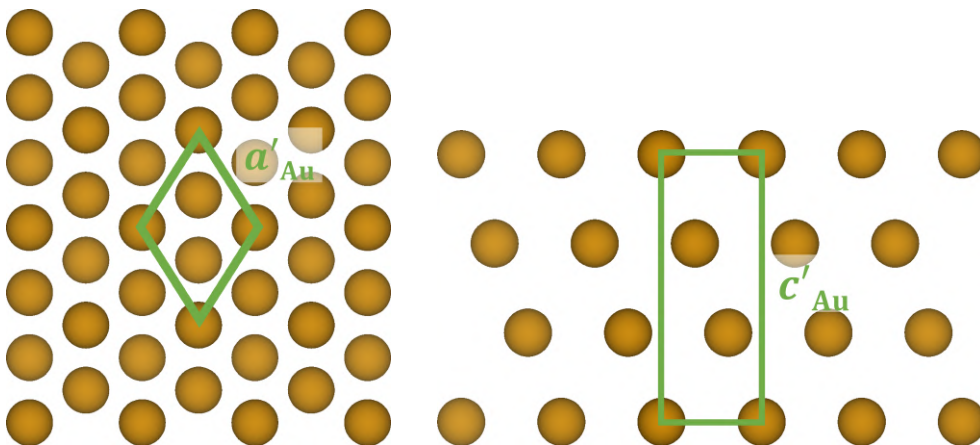


**Figure 4.3:** Adapted unit cell (green) for Au(111) with  $a'_{\text{Au}}$  in top view (left) and  $c'_{\text{Au}}$  in side view (right).

### 4.3 Building the MoS<sub>2</sub>@Au(111) compound

Comparing the lattice constant of MoS<sub>2</sub> with Au(111) there is a difference of 0.31 Å. This results in a biaxial strain of 9% on the gold structure to fit the size of MoS<sub>2</sub>. In this section, we describe two approaches for the construction of a MoS<sub>2</sub> on Au(111) compound. We start with a supercell which is physically reasonable, but computational expensive. Hence, we employ a more feasible approach with the junction constrained to the unit cell of MoS<sub>2</sub>.

#### 4.3.1 Supercell

A possible solution to minimize the strain on gold, is the use of a supercell (sc). Thus, the number of atoms is increased until a satisfying strain value is reached. However, it is important to keep the number of atoms as small as possible to keep the computational costs feasible. Changing the angle between both materials can help decreasing the strain as well. The following supercell was constructed with the program CellMatch [33].

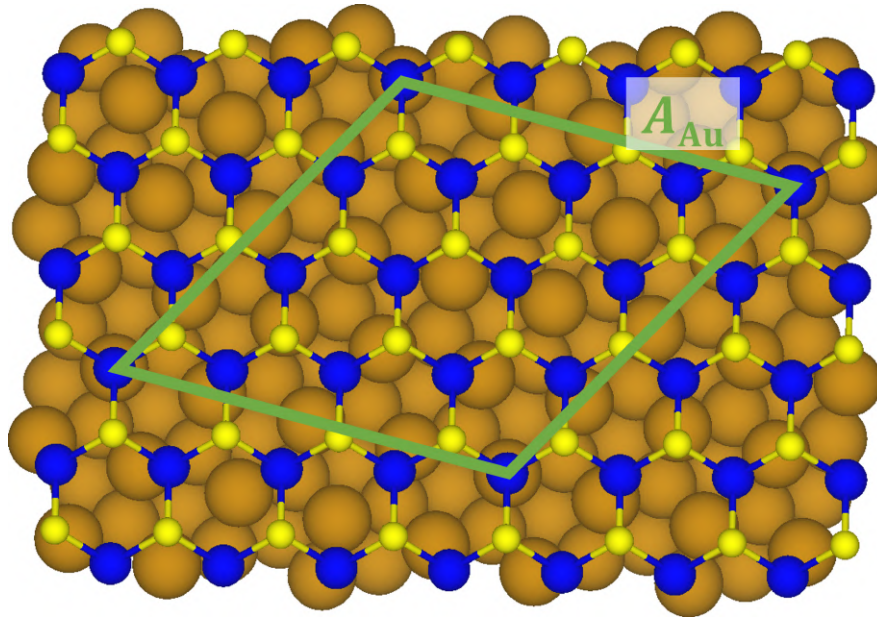


**Figure 4.4:** Supercell with  $(\sqrt{13} \times \sqrt{13})$  MoS<sub>2</sub> on  $(4 \times 4)$  gold with a 0.13% strain on gold. The rotation between MoS<sub>2</sub> and gold is 13°.

A supercell with a strain on Au(111) of 0.13% is shown in Figure 4.4. The angle between both materials is 13°. It contains  $(\sqrt{13} \times \sqrt{13})$  unit cells of MoS<sub>2</sub> and  $(4 \times 4)$  Au(111) unit cells. The number of atomic layers of gold is three. The resulting number of atoms is 87. The distance between the Au(111) substrate and the lower sulfur atoms in the supercell, depicted in Figure 4.5, is  $d_{sc} = 3.29$  Å [34].

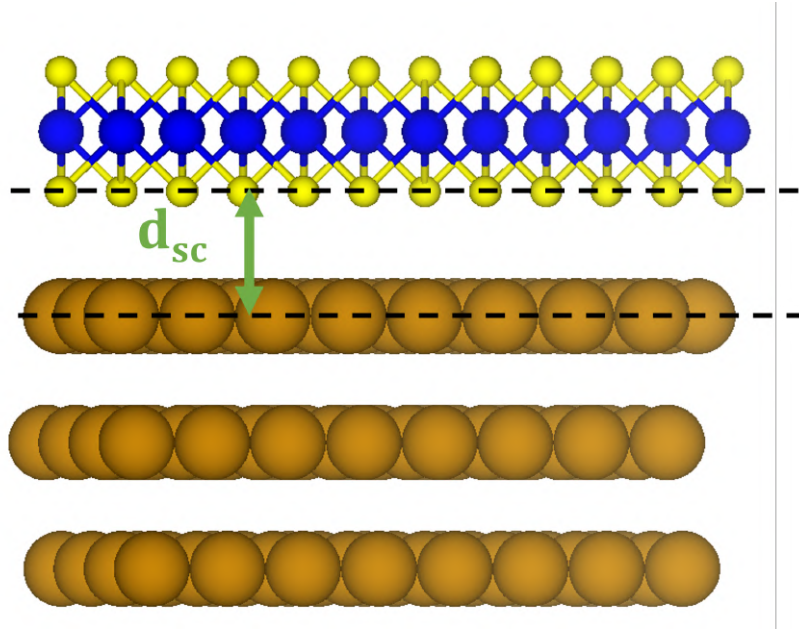


**Figure 4.5:** Distance  $d_{sc}$  between lower sulfur atoms and top gold layer in a  $\text{MoS}_2@Au(111)$  supercell.

### 4.3.2 $\text{MoS}_2$ unit cell matched on Au(111)

The number of atoms in the previously constructed super cell is still large and computationally expensive especially concerning computational methods beyond DFT *e.g.*, GW and BSE. For this reason we used an approach introduced by Bruix *et al.* [34]. A  $(1 \times 1)$   $\text{MoS}_2$  unit cell is matched on the strained  $(1 \times 1)$  Au(111) unit cell in three different configurations. Therefore the position of the  $\text{MoS}_2$  atoms is changed. The three different geometries are shown in Figure 4.6. The distances between the monolayer and substrate are taken from [34]. In the first system the sulfur atoms are placed on top of the gold atoms. For the second one the molybdenum atoms are placed on top of the gold atoms and will be labeled as face centered crystal-like configuration (fcc). The third geometry is labeled as hexagonal closed-packed configuration (hcp) since the molybdenum and sulfur atoms are placed centered on the Au(111) unit cell. The distance between  $\text{MoS}_2$  and the Au(111) substrate, taken from the literature, is  $d_{\text{ontop}} = 2.51 \text{ \AA}$  for the *ontop* configuration, and  $d_{\text{fcc}} = 3.20 \text{ \AA}$  and  $d_{\text{hcp}} = 3.03 \text{ \AA}$  for the fcc and hcp geometries respectively. In this matched systems the strain on Au(111) is 9%. Since, we are interested in the screening effects and band gap renormalization, it is not reasonable to apply a strain on  $\text{MoS}_2$  to fit the lattice parameter of Au. The band gap of pristine  $\text{MoS}_2$  has a shift from direct to indirect band gap, when a strain is applied. Furthermore, pristine  $\text{MoS}_2$  tends to become metallic for a large strain of about 10% as shown in appendix B as well as in Ref. [35]. Though, a strain of 9% on gold is not physical it provides insight in the influence of gold on the electronic and optical properties of  $\text{MoS}_2$ . Furthermore, a supercell could be regarded as a superposition of the three configurations.

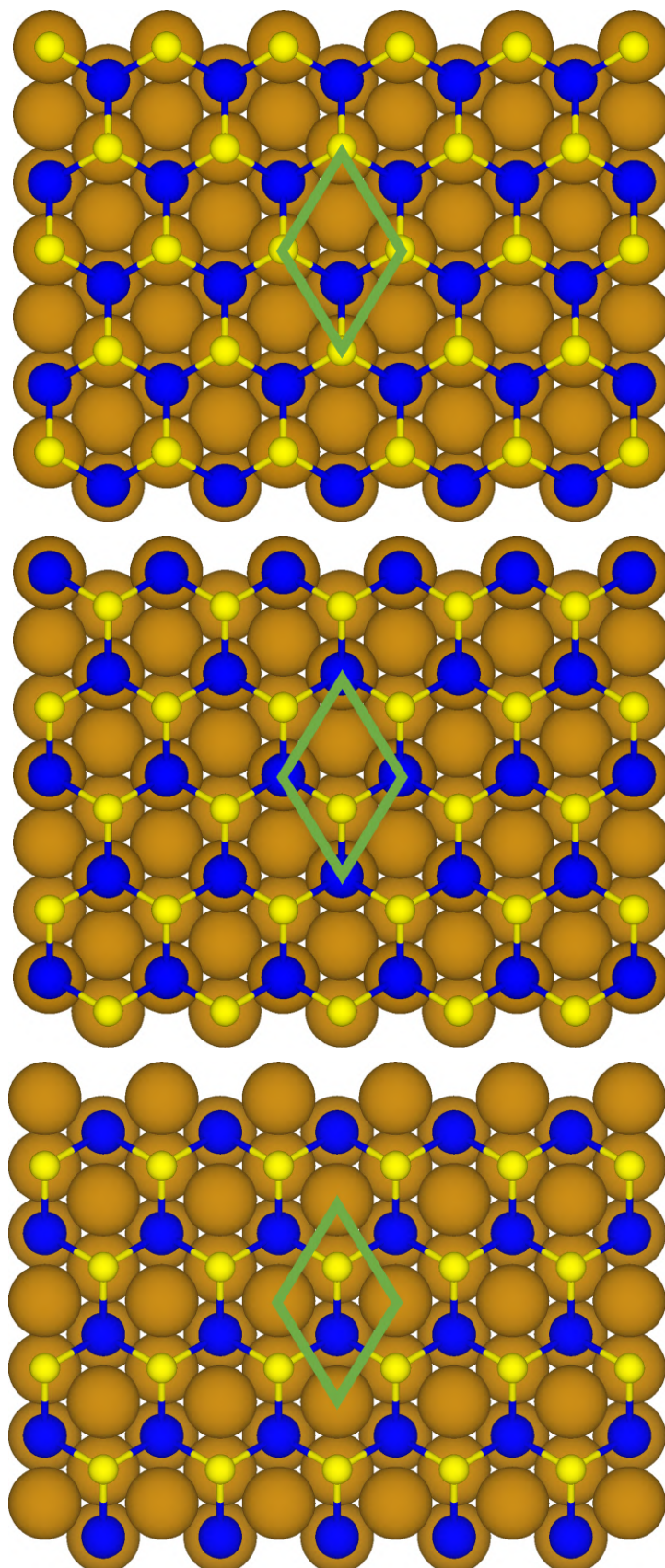


**Figure 4.6:** Adapted matched unit cells for MoS<sub>2</sub> on gold substrate. Upper left: Ontop configuration. Upper right: fcc configuration. Lower left: hcp configuration.



## Results

In this chapter, the results of the MoS<sub>2</sub> on top of Au(111) are compared to pristine MoS<sub>2</sub>. First, we show the results of the DFT calculations. Furthermore, the electronic band gap calculated with *GW* approximation will be analyzed for MoS<sub>2</sub>@Au(111) in hcp configuration. Finally, coming from the *GW* approximation, the absorption spectra and excitonic wave function computed with BSE will be investigated. In this work, the exciting release *nitrogen-14* is used to compute DFT,  $G_0W_0$ , and BSE results.

### 5.1 Structural parameters

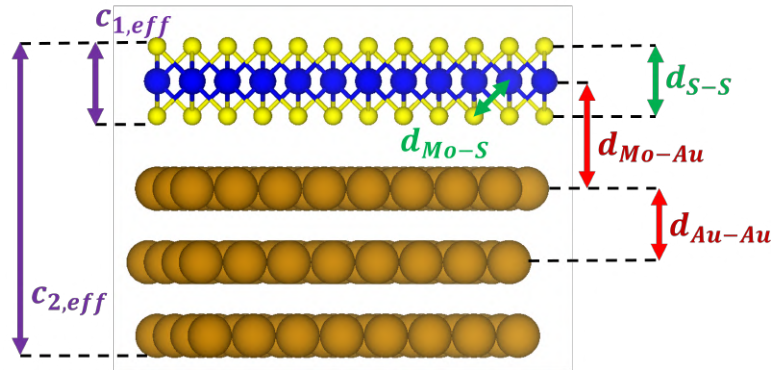


**Figure 5.1:** Distance  $d_{S-S}$  between the upper and lower S atoms in red and distance  $d_{Mo-S}$  between Mo and S in green. The effective thicknesses  $c_{1,eff}$  of pristine MoS<sub>2</sub> and  $c_{2,eff}$  of MoS<sub>2</sub>@Au(111), both in violet.

The optimized lattice constant of MoS<sub>2</sub> is 3.19 Å. The bond length between molybdenum and the sulfur atoms is  $d_{Mo-S} = 2.17$  Å. The distance between both sulfur atoms is  $d_{S-S} = 3.14$  Å. The effective thickness of pristine MoS<sub>2</sub> is  $c_{1,eff} = 5.32$  Å. The optimized unit cell of MoS<sub>2</sub> was used in all substrate configurations without further relaxation of the combined materials. Different gold layers are separated by  $d_{Au-Au} = 2.35$ . The effective thickness of MoS<sub>2</sub>/Au(111) is  $c_{2,eff} = 13.35$  Å. Note

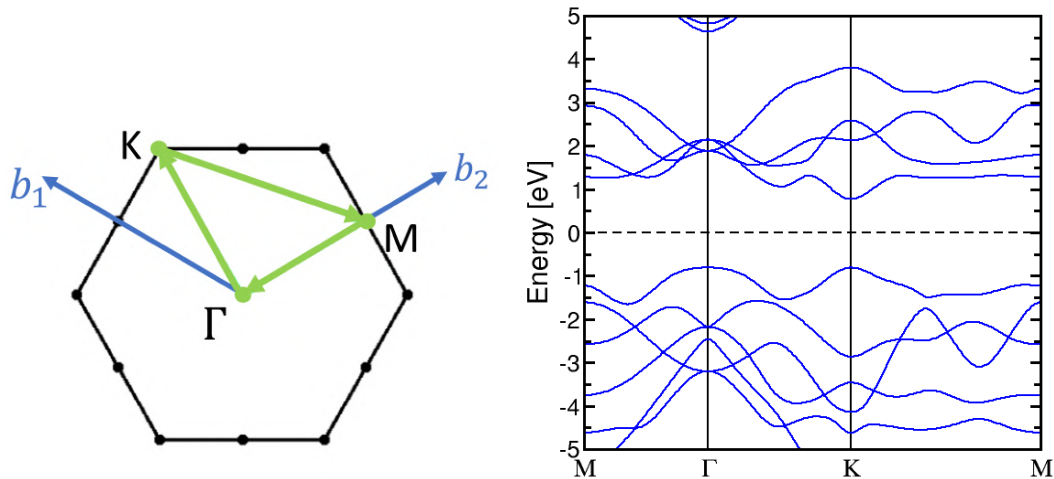
that the effective thickness takes the MT radii into account. The distances and effective thicknesses are shown in Figure 5.1. The distances between MoS<sub>2</sub> and the upper Au layer depend on the used geometry and are given in section 4.3.

## 5.2 Electronic structure

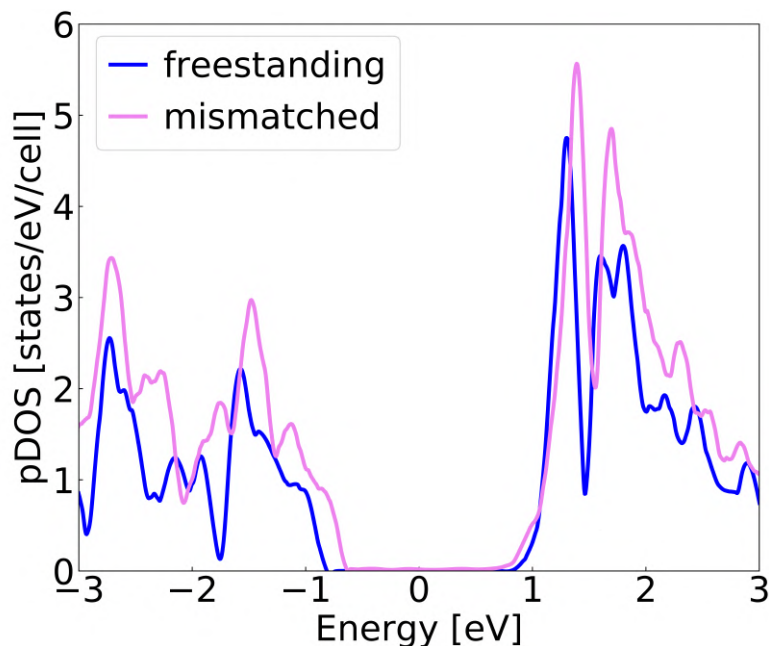
Here, the density of states (DOS) and the band structure from pristine MoS<sub>2</sub>, within the mismatched and matched configurations of MoS<sub>2</sub>@Au(111), are computed with the DFT and the  $G_0W_0$ . For that purpose, the density of states for MoS<sub>2</sub> in the heterostructure is projected onto the MoS<sub>2</sub> layer. In the following, we describe these as the projected density of states (pDOS).

### 5.2.1 Kohn-sham band structure and pDOS

The KS band structure of the pristine MoS<sub>2</sub> along the M- $\Gamma$ -K-M path is shown in Figure 5.2. The calculated band gap at the K-point is 1.58 eV. This is in good agreement with the literature where the value is between 1.5 to 1.8 eV [34, 36–38]. Nevertheless, the KS band gap is underestimated, as stated in Chapter 2.



**Figure 5.2:** Top: Brillouin zone for MoS<sub>2</sub>. The symmetry points are marked with green dots. The blue arrows mark the reciprocal vectors. Bottom: Band structure for MoS<sub>2</sub> with the symmetry points  $\Gamma$ , M, and K.



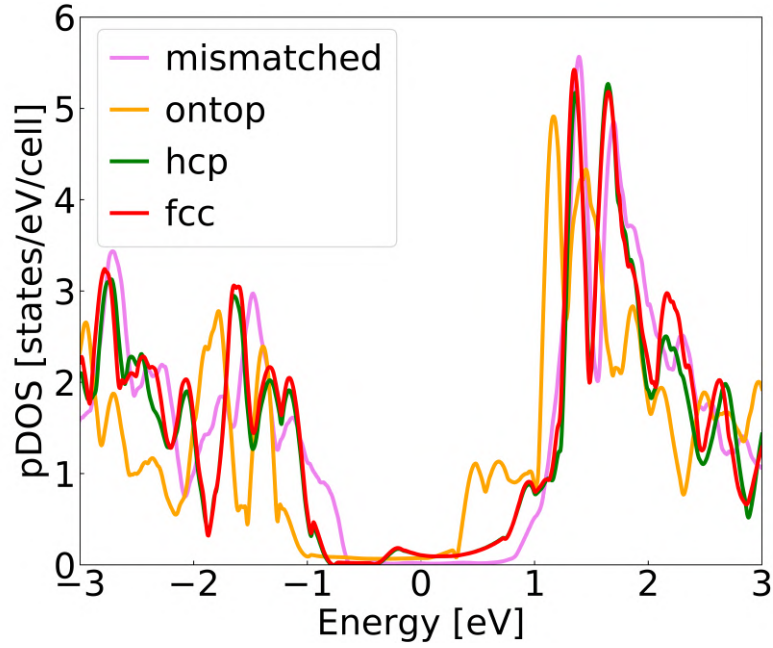
**Figure 5.3:** Projected density of states of pristine MoS<sub>2</sub> compared to the supercell.

Figure 5.3 shows the density of states projected onto the MoS<sub>2</sub> structure for the supercell compared to the pristine structure. Figure 5.4 and 5.5 show the three different matched geometries compared to the pDOS of the supercell and the freestanding MoS<sub>2</sub>. The overall shape of all pDOS is similar. Comparing the pDOS of the supercell with the matched configurations, the supercell seems to be a mixture of all three geometries. However, the supercell has the most fitting similarity to pristine MoS<sub>2</sub> regarding its shape. This is reasonable due to the smaller strain on the Au(111) structure. Whereas, the strain of 9 % on gold in the matched geometries is rather nonphysical. Nevertheless, they give an insight into the substrate effects on the KS band gap. The resulting band gaps are listed in Table 5.1.

The Figures 5.4 and 5.5 show the band gap of the heterostructures is not zero. We describe these as noise. This contradicts the characteristic of a semiconductor. To evaluate the size of the band gap for MoS<sub>2</sub>@Au(111) in the mismatched configuration, a threshold of 0.03 for the density of states was applied. This threshold matches the turning points in the curve where the conduction band minimum (CBm) and valence band maximum (VBM) are estimated. For the matched geometries, the threshold was set to 0.3 because of the higher noise in the estimated band gap. The band gap in the pDOS of the supercell is reduced by 0.1 eV compared to the band gap of pristine MoS<sub>2</sub> and has a size of 1.48 eV. With the applied threshold for the matched geometries, the band gap is 1.6 eV for the fcc and hcp structure and 1.48 eV for the ontop configuration. The smaller band gap in ontop geometry indicates that covalent bonds are formed between MoS<sub>2</sub> and the gold atoms. In contrast, the interaction in the fcc and hcp geometries is weak. The fcc and hcp geometries' resemblance to the pDOS of the supercell is more significant than the ontop geometry.

**Table 5.1:** KS band gap for pristine MoS<sub>2</sub> and MoS<sub>2</sub>@Au(111) supercell with the applied strain on Au(111), respectively.

	Method	MoS <sub>2</sub>	MoS <sub>2</sub> @Au(111)	
		$E_g$ in eV	$E_g$ in eV	strain in %
Present work	(PBE)	1.58	1.48	0.13
			1.48	9.0 (ontop)
			1.60	9.0 (hcp and fcc)
Ref. [34]	(PBE)	1.58	1.61	0.15
			1.56	9.0 (hcp and fcc)
Ref. [39]	(LDA)	1.88	1.87	
Ref. [36]	(LDA)	1.80	1.85	6.3



**Figure 5.4:** Projected density of states of MoS<sub>2</sub> for different geometries with 3 atomic layers of Au compared to the mismatched structure.

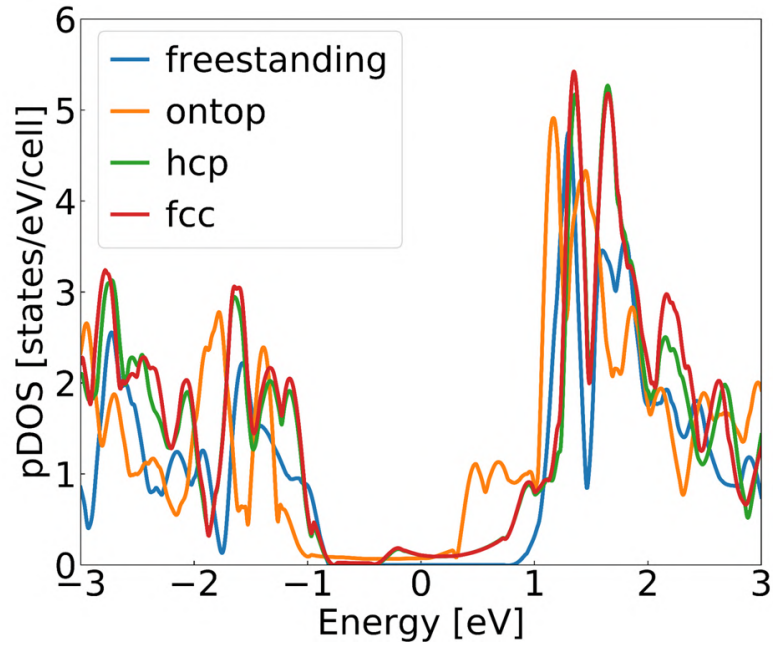


**Figure 5.5:** Projected density of states of MoS<sub>2</sub> for different geometries with 3 atomic layers of Au compared to pristine MoS<sub>2</sub>.

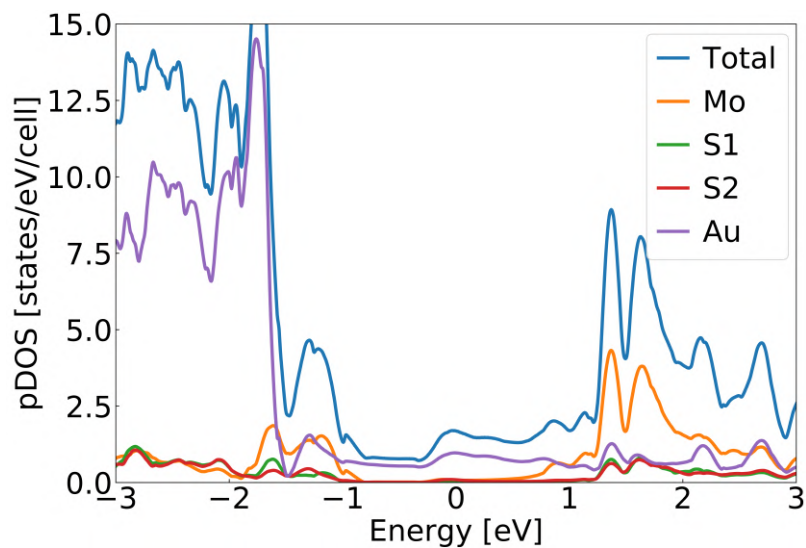


**Figure 5.6:** Projected density of states of Mo, S, and Au states in hcp geometry

Figure 5.6 shows the total density of states of MoS<sub>2</sub>@Au(111) and the contribution of the atoms of Au, Mo, and S states in hcp geometry. The edges of the band gap are determined through Mo, marked in orange. The Au states dominate the deep states with energy below -1.5 eV. To understand the pDOS of MoS<sub>2</sub> better, we split the pDOS further and calculate the s-, p-, and d-orbitals.

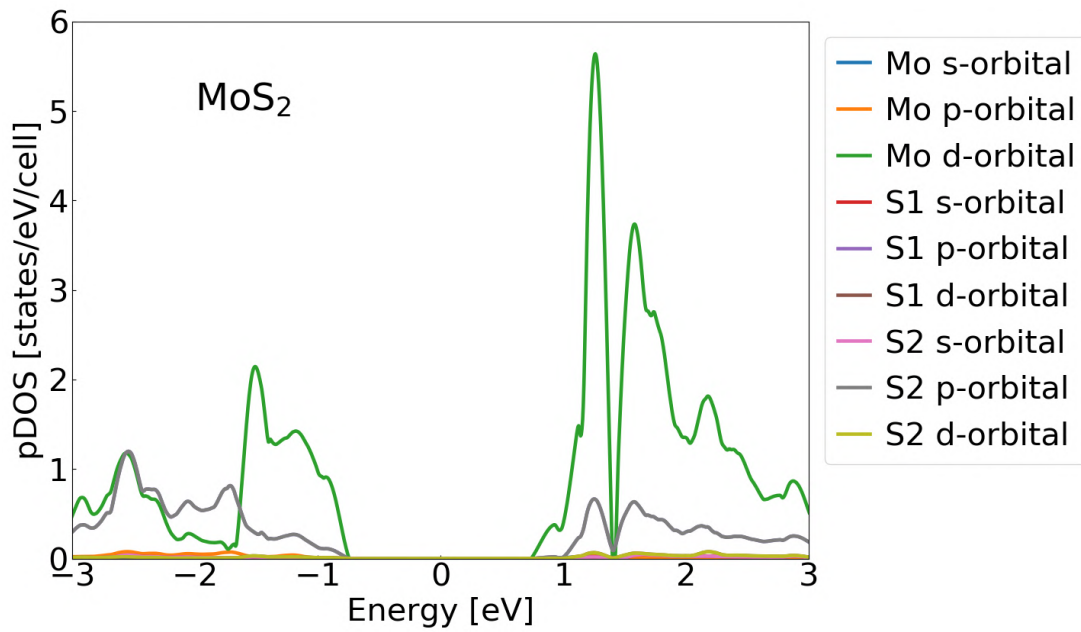


**Figure 5.7:** Projected density of states of s-,p-,and d-orbitals of Mo and S in pristine MoS<sub>2</sub>.

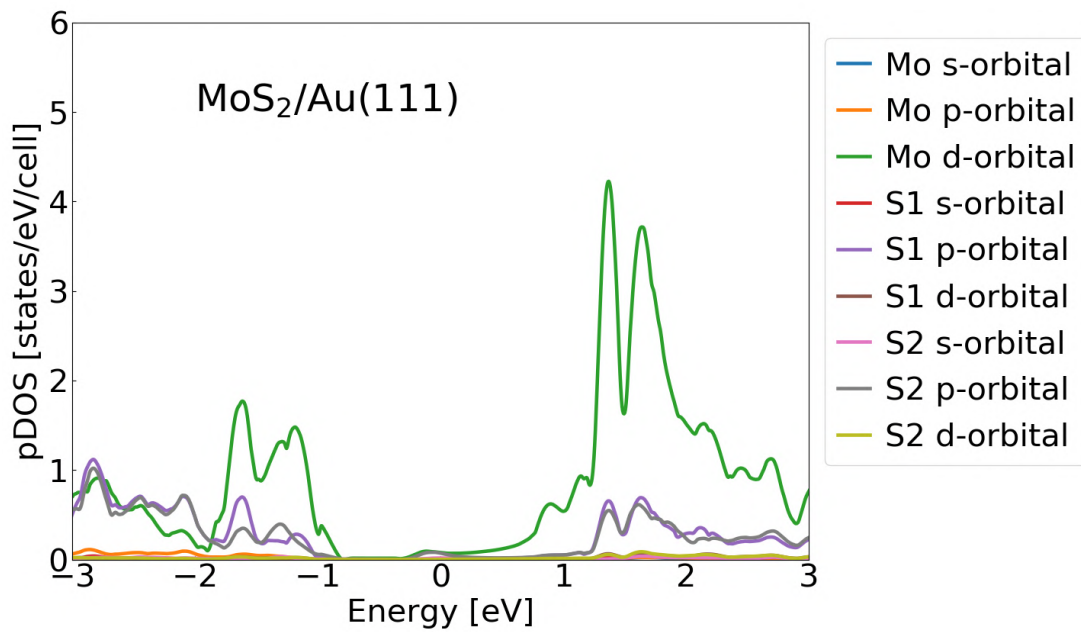
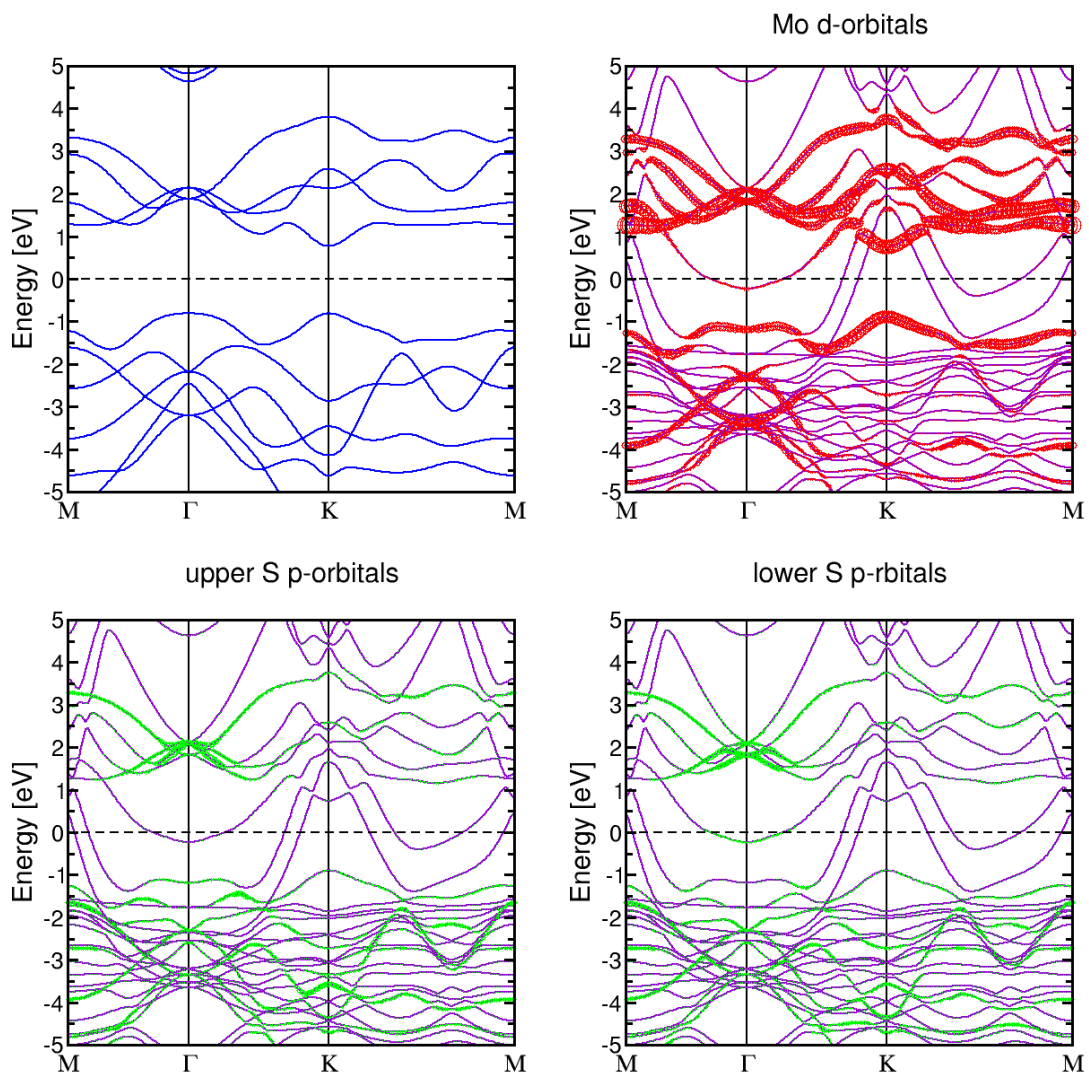


**Figure 5.8:** Projected density of states of s-,p-,and d-orbitals of Mo and S for MoS<sub>2</sub>@Au(111) in hcp geometry.

The contribution of the different orbitals of MoS<sub>2</sub> can be seen in Figure 5.7 and 5.8. The top image illustrates the orbitals in the pristine structure. The bottom one depicts

the part from the MoS<sub>2</sub> orbitals in the heterostructure. The d-orbitals of Mo have the highest impact on the pDOS in both structures. Furthermore, the d-orbitals form the CBM and VBM of the semiconductor. In contrast, the effects of the other orbitals from Mo are small. Regarding the sulfur atoms, the p-orbitals contribute to the pDOS. Since the lower S-atoms are more influenced by the Au substrate, the p-orbitals atoms differ compared to the pristine case.

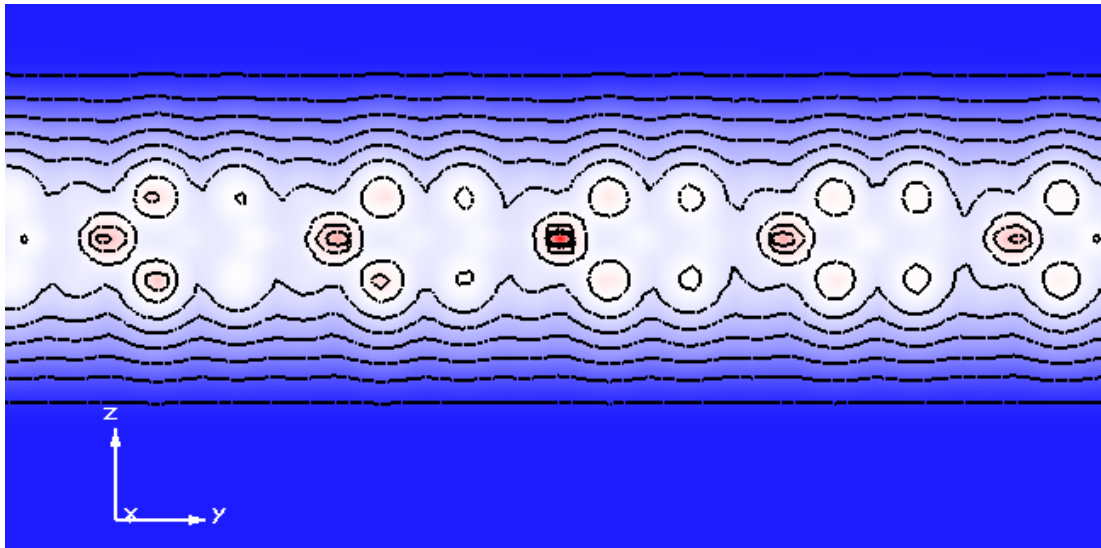
Figure 5.9 shows the band structure with the contributing orbitals of Mo and S in the compound compared to the pristine material. The d-orbitals are denoted with red dots in the top right figure. We see the direct band gap at the K-point as expected. However, as indicated in the pDOS, the band gap in the MoS<sub>2</sub>@Au(111) junction is not zero due to the electronic hybridization between Au and the d-orbitals of Mo. In Figure 5.9, these other states with smaller weights are depicted as small red dots. The strong hybridization between the metal and the Mo d-orbitals is also observed in the literature [39].



**Figure 5.9:** Kohn-sham band structure of pristine MoS<sub>2</sub> (top left) and projected band structure of MoS<sub>2</sub>@Au(111) in hcp geometry for the Mo d-orbitals (top right) and sulfur p-orbitals (bottom left and right).

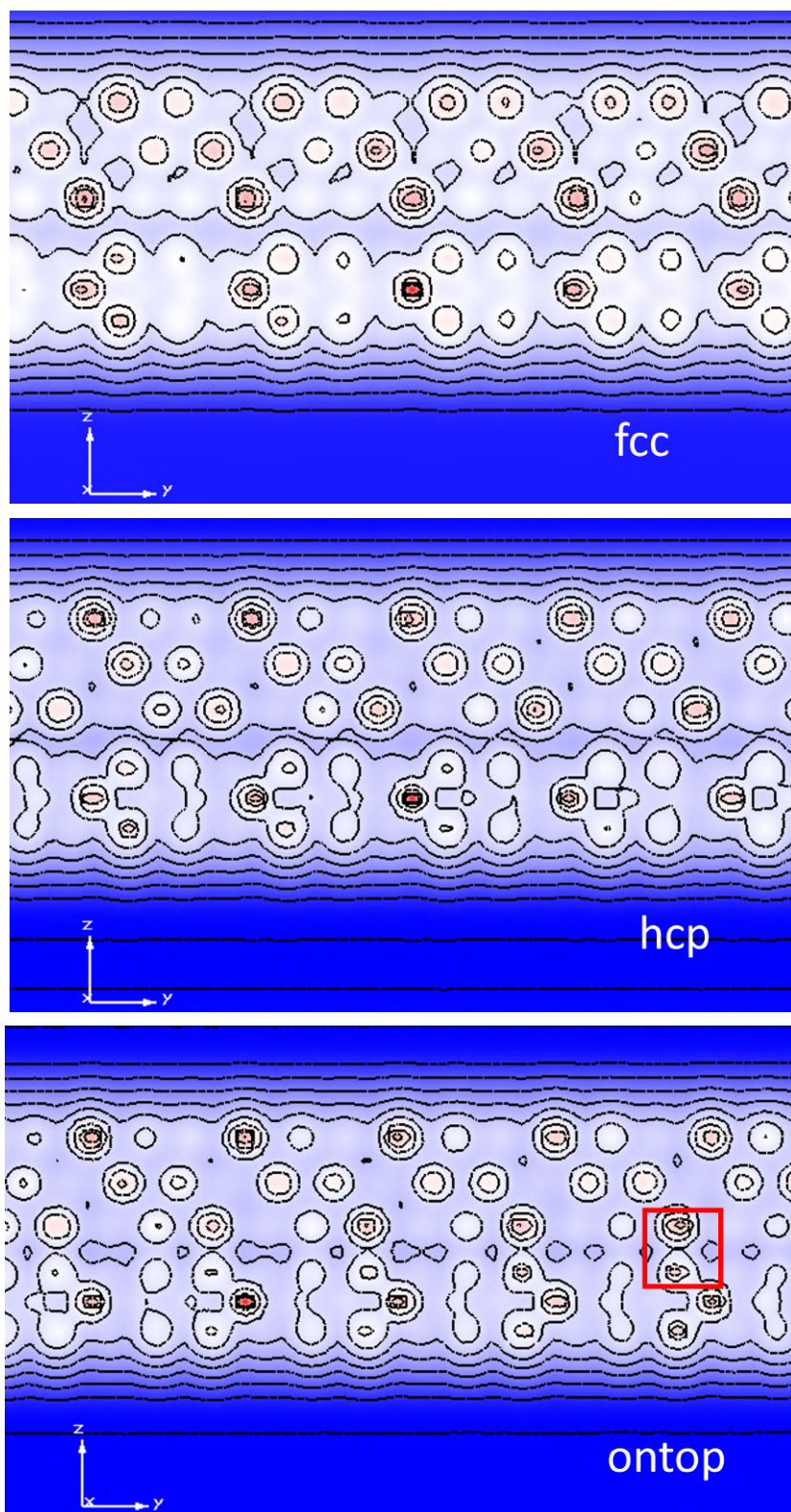
### 5.2.2 Charge density distribution

In the following part, we present the effect on the charge density distribution of a gold substrate on MoS<sub>2</sub>. In Figure 5.10, the charge density of pristine MoS<sub>2</sub> is shown, where the circles in the center layer depict the charge density of the Mo atoms sandwiched by the two S atoms. The blue areas indicate charge density of value zero. The red dots present a charge density of high value.



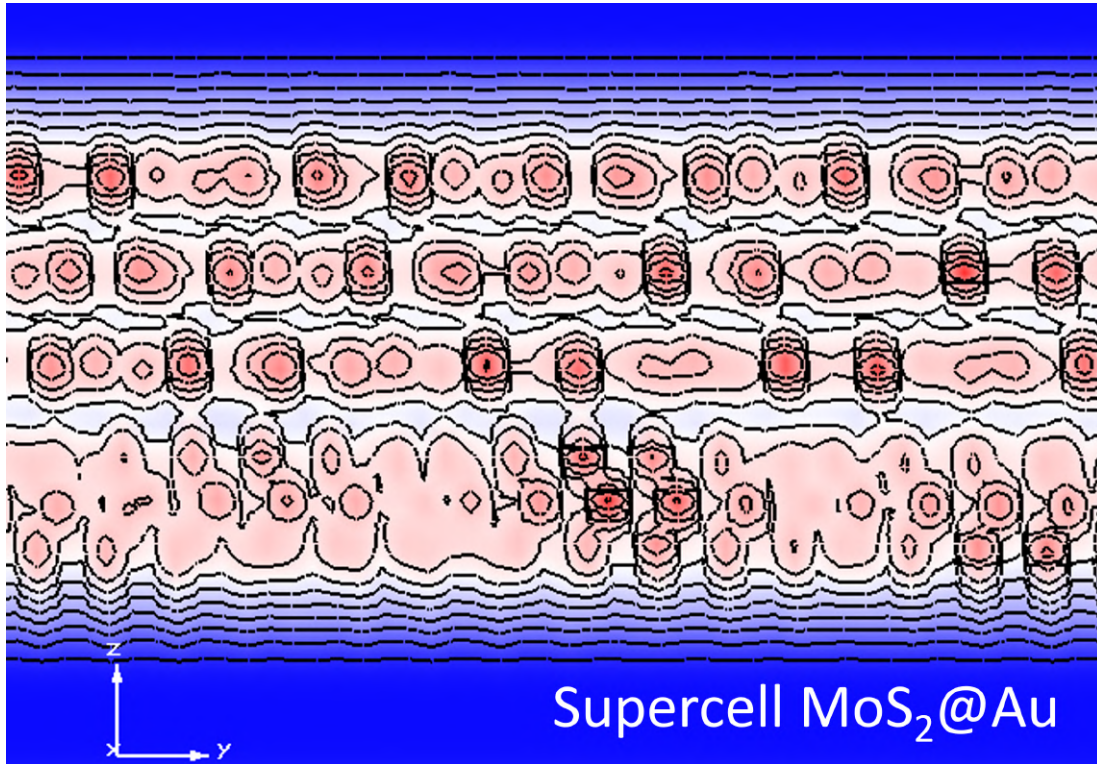
**Figure 5.10:** Charge density distribution for MoS<sub>2</sub>.

Figure 5.11 shows a further indication of the strong interaction in the ontop configuration. As can be seen in the top and center figure, MoS<sub>2</sub>@Au(111) in fcc and hcp geometry show less interaction between the MoS<sub>2</sub> and Au layers. In contrast, the ontop configuration shows a high interaction between the S atoms with the upper Au layer, highlighted with a red square. Consequently, we will continue with the hcp configuration to get more insight into the screening effects of Au(111).



**Figure 5.11:** Top: Charge density distribution for MoS<sub>2</sub>@Au(111) in fcc geometry. Center: Charge density distribution for MoS<sub>2</sub>@Au(111) in hcp geometry. Bottom: Charge density distribution for MoS<sub>2</sub>/Au(111) in ontop geometry. The red square marks strong interaction between Au and S atoms in ontop configuration.

Figure 5.12 shows the charge density distribution of  $\text{MoS}_2@Au(111)$  in the mismatched configuration. It can be interpreted as a superposition of the charge density distributions from the different geometries depicted in Figure 5.11. Some areas present a strong interaction between the Au and S atoms. On the other hand, there are areas with small interactions similar to the hcp and fcc structures.

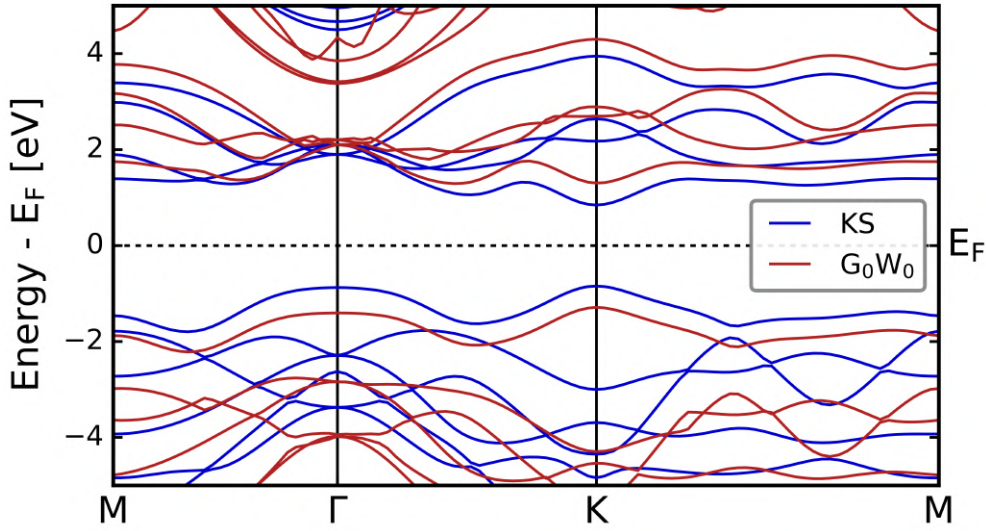


**Figure 5.12:** Charge density distribution for  $\text{MoS}_2@Au(111)$  in the mismatched structure.

### 5.2.3 Electronic properties from $G_0W_0$

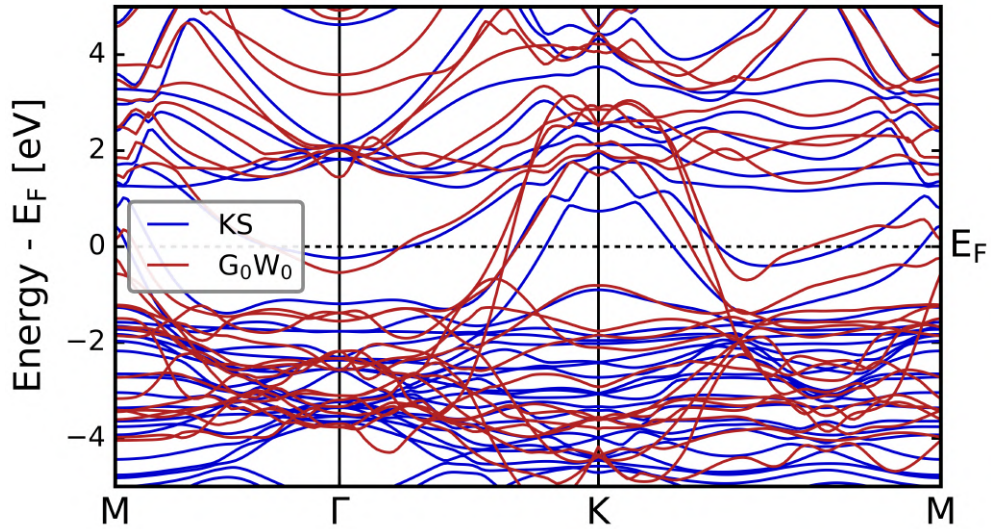
In this section, we present the results for the electronic structure in  $G_0W_0$  approximation. In the previous section, we have shown that the interaction between MoS<sub>2</sub> and the gold substrate is weak for the hcp and fcc geometry but has a covalent bonding in the ontop configuration. Consequently, we will continue with the hcp configuration to get more insight into the screening effects of Au(111).

Figure 5.13 shows the quasi-particle band structure for pristine MoS<sub>2</sub> (red line). For comparison, the KS band structure is plotted, too. The direct band gap at the K-point is preserved as expected. But the band gap is increased by 1.23 eV and is calculated to be 2.81 eV. This coincides with reference values in the literature of 2.7 up to 2.9 eV [34, 36, 40, 41] for pristine MoS<sub>2</sub> with  $GW$ . The band gap strongly depends on the used  $\mathbf{k}$ -grid mesh, which is  $18 \times 18 \times 1$ .



**Figure 5.13:** Band structure for pristine MoS<sub>2</sub> in  $G_0W_0$  approximation (red) and the KS band structure (blue).

Analogously, we calculated the electronic band structure for MoS<sub>2</sub>@Au(111) in hcp geometry with the  $G_0W_0$  approach. Figure 5.14 depicts the quasi-particle and KS band structures. Again, we observe a band gap rise at the K valley of MoS<sub>2</sub>. It yields 2.18 eV, which is a decrease of 0.70 eV compared with the KS band gap. Nevertheless, just the conduction band minimum of MoS<sub>2</sub> is raised. The valence band maximum is not changed as much. The calculated band gap is in good agreement with the literature given with 2.3 eV for MoS<sub>2</sub> on Au [36], too. Of course, it is to be expected that the band gap depends on the stacking of MoS<sub>2</sub>@Au(111) and on the size of the strain applied on the substrate, such as observed at the DFT level. Experimental measurements performed with angle-resolved photoelectron spectroscopy (ARPES) in Park *et al.* [42] give the band gap at the K-point with 1.90 eV, which is smaller than ours by 0.28 eV.



**Figure 5.14:** Band structure for MoS<sub>2</sub>/Au(111) with hcp geometry in  $G_0W_0$  approximation (red) and the KS band structure (blue).

The band gap in the pDOS of MoS<sub>2</sub>@Au(111) in  $G_0W_0$  approximation is non-zero, too. It seems that the pDOS in Figure 5.15 is also showing the hybridization effects like before in the KS pDOS.

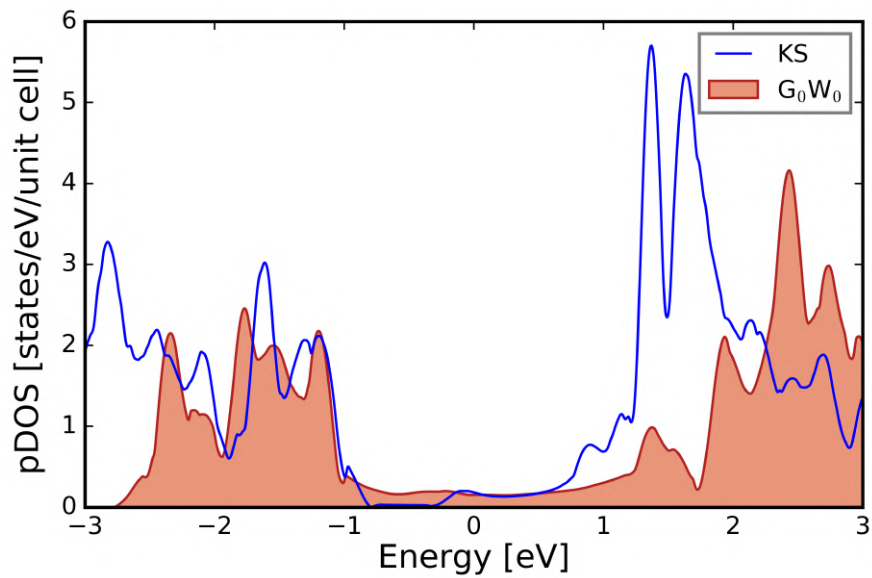


**Figure 5.15:** Projected DOS of MoS<sub>2</sub>@Au(111) in hcp structure in  $GW$  approximation and KS

## 5.3 Optical properties

In this section, we present the results for the optical properties determined with BSE for freestanding  $\text{MoS}_2$  and  $\text{MoS}_2@Au(111)$  in hcp geometry. We investigate the dielectric function and exciton binding energies in the first part. Then, the exciton wave function in real- and k-space for the pristine  $\text{MoS}_2$  and the  $\text{MoS}_2@Au(111)$  junction is analyzed. In each case, the focus is on the first exciton.

### 5.3.1 Dielectric function

Figure 5.16 shows the components of the in-plane imaginary and real parts of the macroscopic dielectric functions. The red curve presents the  $\text{MoS}_2@Au(111)$  compound. The blue line is the dielectric function of pristine  $\text{MoS}_2$ . All components of the dielectric functions were rescaled with Eq. 3.8. For freestanding  $\text{MoS}_2$ , we identified the first three excitons, marked with A, B, and C. The absorption onset of pristine  $\text{MoS}_2$  in the top panel in Figure 5.16 is at about 2.4 eV. The onset corresponds to the transition between VBM and CBm at the K-point. More precisely, we obtain an optical transition of 2.4 eV for the exciton A. Exciton B originates from the transition between the CBm and VBM at the K point and corresponds to the peak at about 2.6 eV. With the binding energy  $E_b$  being the difference between the electronic band gap and optical transition energy, we gain 0.4 eV for the exciton A in pristine  $\text{MoS}_2$ . For the  $\text{MoS}_2@Au(111)$  junction, we obtain 0.2 eV for the exciton binding energy. This is a reduction of 0.2 eV compared to the freestanding monolayer. Experimental measurements done by Park *et al.* received 0.1 eV for the electron binding energy [42]. The results are listed in Table 5.2.

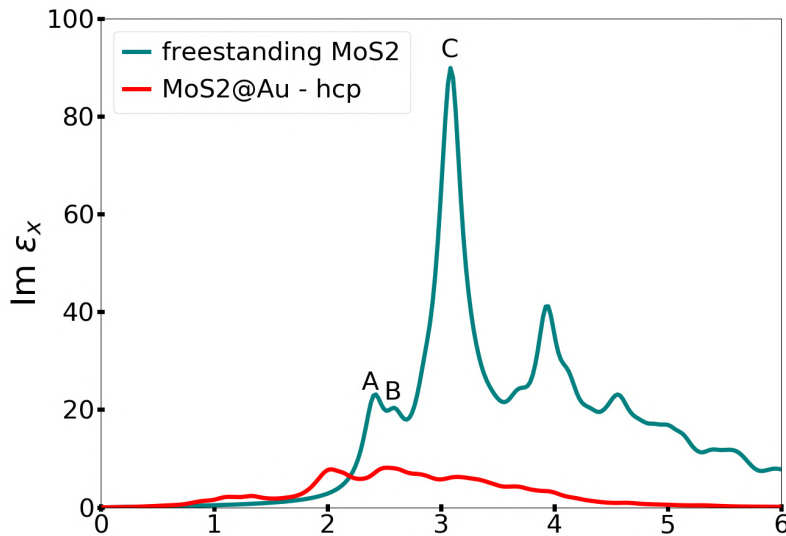


**Figure 5.16:** Imaginary part of the in-plane macroscopic dielectric function of pristine  $\text{MoS}_2$  and  $\text{MoS}_2$  on gold in hcp configuration.

**Table 5.2:** Electronic and optical band gap for pristine MoS<sub>2</sub> and MoS<sub>2</sub>@Au(111) supercell from BSE within GW.

	MoS <sub>2</sub>			MoS <sub>2</sub> @Au(111)		
	$E_g^{\text{el}}$ in eV	$E_g^{\text{opt}}$ in eV	$E_B$ in eV	$E_g^{\text{el}}$ in eV	$E_g^{\text{opt}}$ in eV	$E_B$ in eV
Present work	2.8	2.4	0.4	2.2	2.0	0.2
ARPES [42]				2.0	1.9	0.1

The overall shape of the imaginary part of the dielectric function of MoS<sub>2</sub>@Au(111) is smoothed. This effect also shows in the reflectance spectra of MoS<sub>2</sub>@Au(111) in Ref. [42]. These effects suggest a strong screening from the metallic substrate. The smoothed curve of MoS<sub>2</sub>@Au(111) makes a direct comparison with the one of the pristine MoS<sub>2</sub> difficult. Also, the smoothed curve featured smearing of the peaks complicates the interpretation. We presume the peak at about 2 eV corresponds with the transition in the MoS<sub>2</sub> layer of MoS<sub>2</sub>@Au(111). This value is smaller than the calculated optical band gap of about 2.2 eV. Nevertheless, both values share the same order of magnitude.

The real part of the macroscopic dielectric function in Figure 5.17 shows a peak at about 2.4 eV, which corresponds to the first exhibit exciton A in the imaginary part. The second and third peak coincide with exciton B and C, respectively. The same features are also presented by the real part of the dielectric function of MoS<sub>2</sub>@Au(111). Both curves change sign at about 3.2 eV.

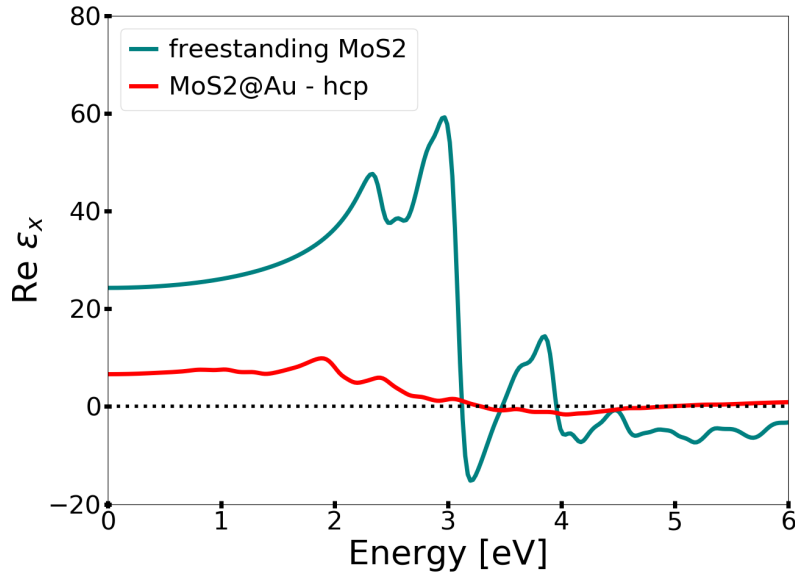


**Figure 5.17:** Real part of the in-plane macroscopic dielectric function of pristine MoS<sub>2</sub> and MoS<sub>2</sub> on gold in hcp configuration.

Figure 5.18 depicts the out-of-plane imaginary part of the macroscopic dielectric function of pristine MoS<sub>2</sub> and MoS<sub>2</sub>@Au(111) compound. The quantum confinement of the electronic wave function causes a constraint on the out-of-plane exciton in two-dimensional materials like MoS<sub>2</sub> [43]. Due to this limitation in dimensionality, the imaginary part of the macroscopic dielectric function in the out-of-plane direction presents an exceedingly weak absorption, which exhibits in other TMDs, too [44]. The onset of the curve is at about 3.5 eV. In contrast to the in-plane case, the out-of-plane direction shows a rise in the dielectric function for MoS<sub>2</sub>@Au(111). This suggests an increased absorption. The real part of the dielectric function, depicted in Figure 5.19, shows similar features like the imaginary part. There is no change in sign, neither for the pristine nor the compound material.

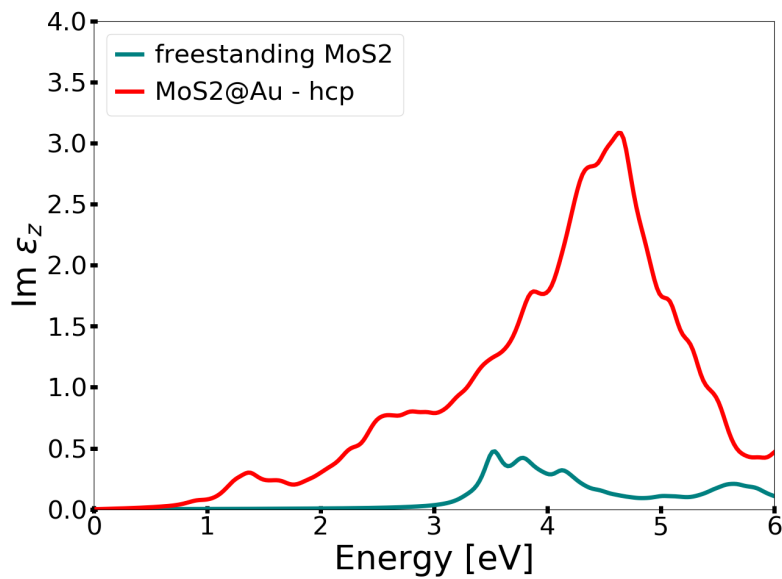


**Figure 5.18:** Imaginary part of the macroscopic dielectric function in out-of-plane direction of pristine MoS<sub>2</sub> and MoS<sub>2</sub>@Au(111) in hcp configuration.

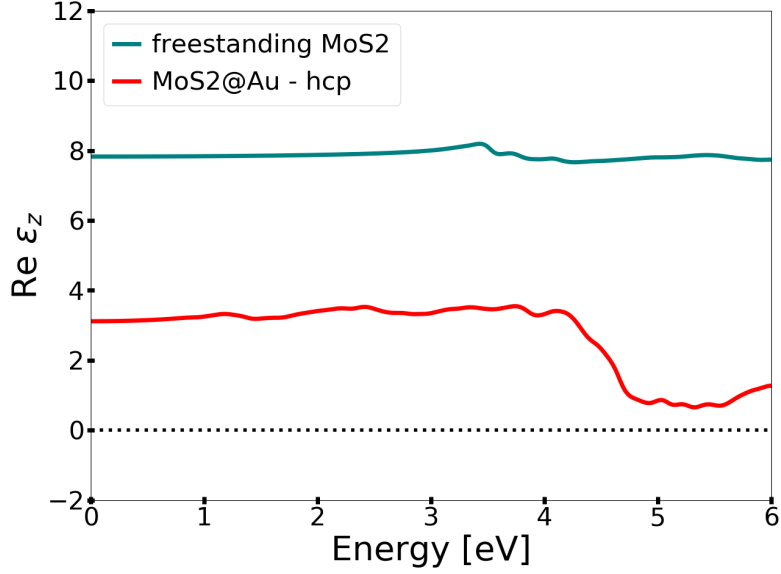


**Figure 5.19:** Real part of the macroscopic dielectric function in out-of-plane direction of pristine MoS<sub>2</sub> and MoS<sub>2</sub>@Au(111) in hcp configuration.

### 5.3.2 Exciton wave function

In this section, we analyze the first appearing exciton in the MoS<sub>2</sub> layer by investigating the probability density isosurface of the electron part of the exciton in the real space and the excitonic weights in the k-space for both the pristine material and MoS<sub>2</sub>@Au(111) heterostructure.

In Figure 5.20 we show the exciton A for pristine MoS<sub>2</sub>. The exciton A is localized at the VBM and CBm around the K-point in the band structure. The red circles in the bottom representation of the KS band structure denote the excitonic weights. The top figure presents the electron part of the exciton in real space with the hole centered at the Mo atom. The blue areas depict the isosurfaces. For the pristine case, the electrons are distributed at the surrounding Mo atoms.

Figure 5.21 shows the same properties for MoS<sub>2</sub>@Au(111) in hcp geometry. To distinguish between the Au states and states of MoS<sub>2</sub>, we check the band structure in the bottom against the representation in Figure 5.9. The exciton in the KS band structure of MoS<sub>2</sub>@Au(111) is localized around the K-point of MoS<sub>2</sub>. Nevertheless, the excitonic weights are distributed along the Au states, too. This effect also shows in the image of the electron distribution in real space. Like the pristine material, the electrons are distributed around the Mo atoms, with the hole fixed at one Mo atom. We also see a slight spreading of the electrons at the Au atoms.

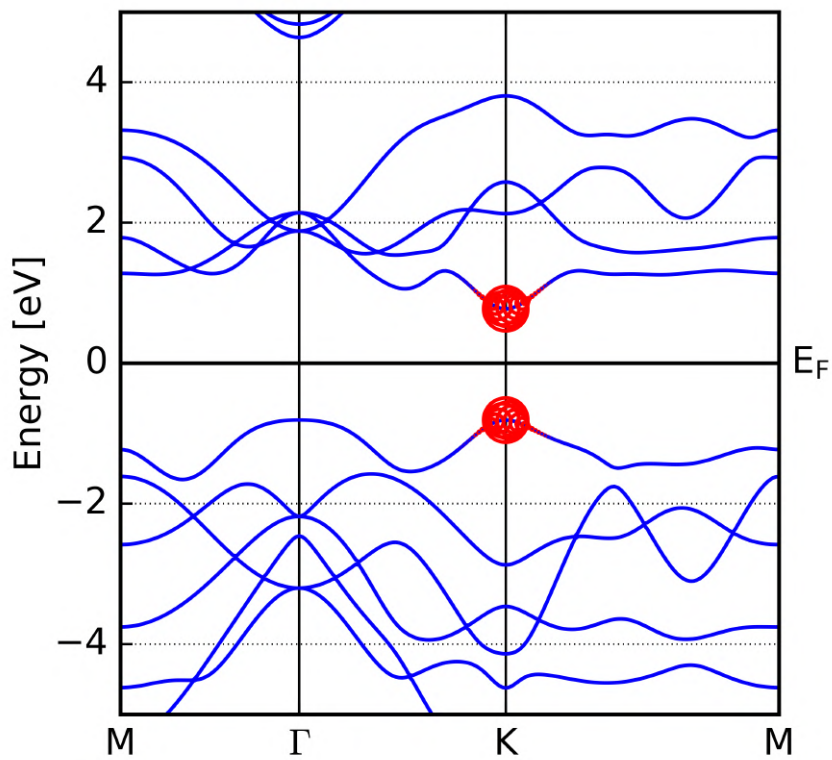
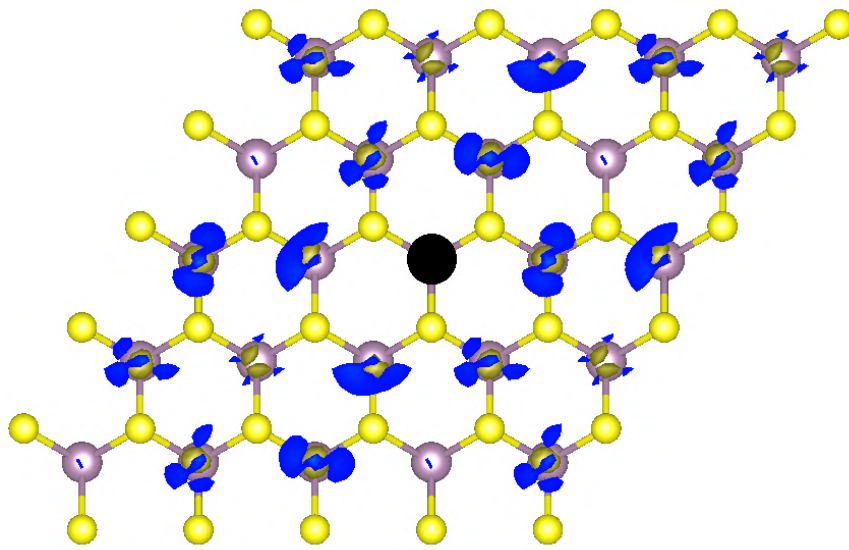


**Figure 5.20:** Exciton A of pristine MoS<sub>2</sub>. Top: Visualization of the electron-hole wave function in real space. The black dot marks the position of the hole. Blue denotes the electron probability. Bottom: Excitonic weights projected onto the KS band structure.

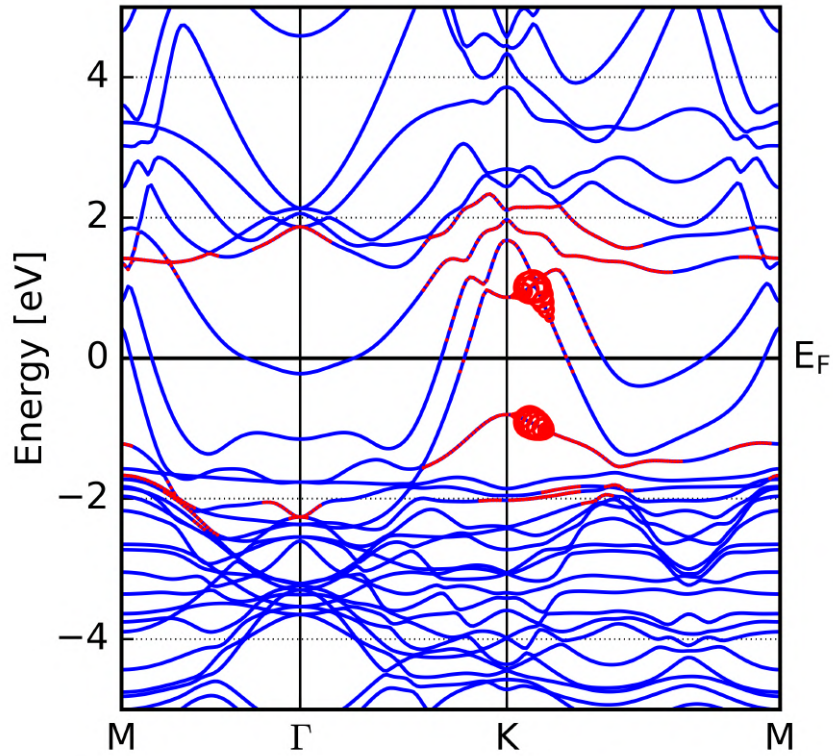
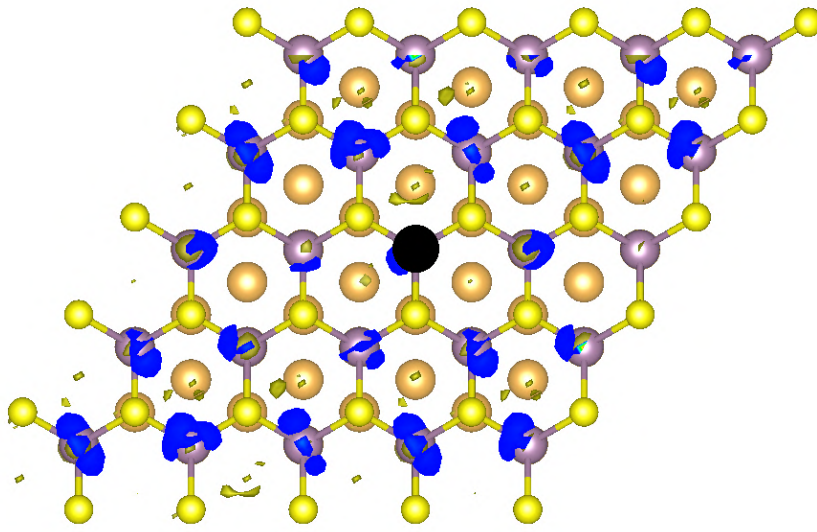


**Figure 5.21:** Exciton of  $\text{MoS}_2@\text{Au}(111)$  in hcp geometry. Top: Visualization of the electron-hole wave function in real space. The black dot marks the position of the hole. Blue denotes the electron probability. Bottom: Excitonic weights projected onto the KS band structure.



---

## Conclusions and outlook

In this work, we investigated the effect of a gold substrate on the electronic and optical properties of monolayer MoS<sub>2</sub>, using first principle calculations implemented in the software package `exciting`.

The KS bandstructure and pDOS for pristine MoS<sub>2</sub> and MoS<sub>2</sub>@Au(111) in hcp, fcc, and ontop geometry have been obtained as well as in the mismatched supercell. All MoS<sub>2</sub>@Au(111) configuration has a decreased band gap at the K-point, which is in good agreement with the existing literature.  $G_0W_0$  calculations also support this impact on the electronic band structure. In addition, the optical properties of MoS<sub>2</sub> and MoS<sub>2</sub>@Au(111) in hcp geometry have been investigated. The imaginary part of the in-plane macroscopic dielectric function for MoS<sub>2</sub>@Au(111) is diminished compared to the pristine material. These suggest a screening from the electrons in the substrate material.

In further extension to this work, the electronic and optical properties for the fcc and ontop geometry should be investigated with  $G_0W_0$  and BSE calculations. Furthermore, the impact of the substrate thickness on the dielectric screening remains to be evaluated.



---

## List of Figures

1.1	Supercell MoS <sub>2</sub> on gold. . . . .	2
2.1	Schematic representation of the self-consistent cycle (adapted from Ref. [15]) . . . . .	6
3.1	Schematic representation of the <b>exciting</b> workflow (adapted from Ref. [11]) . . . . .	13
4.1	Top view (left) and side view (right) of MoS <sub>2</sub> . The primitive unit cell (red) with lattice constant $a$ and the thickness $d$ . . . . .	15
4.2	Face-centered unit cell of gold with (111)-plane (violet). . . . .	16
4.3	Adapted unit cell (green) for Au(111) with $a'_{Au}$ in top view (left) and $c'_{Au}$ in side view (right). . . . .	16
4.4	Supercell with ( $\sqrt{13} \times \sqrt{13}$ ) MoS <sub>2</sub> on ( $4 \times 4$ ) gold with a 0.13% strain on gold. The rotation between MoS <sub>2</sub> and gold is 13°. . . . .	17
4.5	Distance $d_{sc}$ between lower sulfur atoms and top gold layer in a MoS <sub>2</sub> @Au(111) supercell. . . . .	18
4.6	Adapted matched unit cells for MoS <sub>2</sub> on gold substrate. Upper left: Ontop configuration. Upper right: fcc configuration. Lower left: hcp configuration. . . . .	19
5.1	Distance $d_{S-S}$ between the upper and lower S atoms in red and distance $d_{Mo-S}$ between Mo and S in green. The effective thicknesses $c_{1,eff}$ of pristine MoS <sub>2</sub> and $c_{2,eff}$ of MoS <sub>2</sub> @Au(111), both in violet. . . . .	21
5.2	Top: Brillouin zone for MoS <sub>2</sub> . The symmetry points are marked with green dots. The blue arrows mark the reciprocal vectors. Bottom: Band structure for MoS <sub>2</sub> with the symmetry points $\Gamma$ , M, and K. . . . .	22
5.3	Projected density of states of pristine MoS <sub>2</sub> compared to the supercell. . . . .	23
5.4	Projected density of states of MoS <sub>2</sub> for different geometries with 3 atomic layers of Au compared to the mismatched structure. . . . .	24
5.5	Projected density of states of MoS <sub>2</sub> for different geometries with 3 atomic layers of Au compared to pristine MoS <sub>2</sub> . . . . .	25
5.6	Projected density of states of Mo, S, and Au states in hcp geometry . . . . .	25
5.7	Projected density of states of s-,p-, and d-orbitals of Mo and S in pristine MoS <sub>2</sub> . . . . .	26

5.8	Projected density of states of s-,p-,and d-orbitals of Mo and S for MoS <sub>2</sub> @Au(111) in hcp geometry. . . . .	26
5.9	Kohn-sham band structure of pristine MoS <sub>2</sub> (top left) and projected band structure of MoS <sub>2</sub> @Au(111) in hcp geometry for the Mo d-orbitals (top right) and sulfur p-orbitals (bottom left and right). . . . .	28
5.10	Charge density distribution for MoS <sub>2</sub> . . . . .	29
5.11	Top: Charge density distribution for MoS <sub>2</sub> @Au(111) in fcc geometry. Center: Charge density distribution for MoS <sub>2</sub> @Au(111) in hcp geometry. Bottom: Charge density distribution for MoS <sub>2</sub> /Au(111) in ontop geometry. The red square marks strong interaction between Au and S atoms in ontop configuration. . . . .	30
5.12	Charge density distribution for MoS <sub>2</sub> @Au(111) in the mismatched structure. . . . .	31
5.13	Band structure for pristine MoS <sub>2</sub> in $G_0W_0$ approximation (red) and the KS band structure (blue). . . . .	32
5.14	Band structure for MoS <sub>2</sub> /Au(111) with hcp geometry in $G_0W_0$ approximation (red) and the KS band structure (blue). . . . .	33
5.15	Projected DOS of MoS <sub>2</sub> @Au(111) in hcp structure in $GW$ approximation and KS . . . . .	33
5.16	Imaginary part of the in-plane macroscopic dielectric function of pristine MoS <sub>2</sub> and MoS <sub>2</sub> on gold in hcp configuration. . . . .	34
5.17	Real part of the in-plane macroscopic dielectric function of pristine MoS <sub>2</sub> and MoS <sub>2</sub> on gold in hcp configuration. . . . .	35
5.18	Imaginary part of the macroscopic dielectric function in out-of-plane direction of pristine MoS <sub>2</sub> and MoS <sub>2</sub> @Au(111) in hcp configuration. . . . .	36
5.19	Real part of the macroscopic dielectric function in out-of-plane direction of pristine MoS <sub>2</sub> and MoS <sub>2</sub> @Au(111) in hcp configuration. . . . .	37
5.20	Exciton A of pristine MoS <sub>2</sub> . Top: Visualization of the electron-hole wave function in real space. The black dot marks the position of the hole. Blue denotes the electron probability. Bottom: Excitonic weights projected onto the KS band structure. . . . .	38
5.21	Exciton of MoS <sub>2</sub> @Au(111) in hcp geometry. Top: Visualization of the electron-hole wave function in real space. The black dot marks the position of the hole. Blue denotes the electron probability. Bottom: Excitonic weights projected onto the KS band structure. . . . .	39
6.1	Band edges at the K-point of MoS <sub>2</sub> under biaxial strain. . . . .	45
6.2	Band gap at the K-point of MoS <sub>2</sub> @Au(111) under biaxial strain. . . . .	46

---

## Appendix A: Effect of biaxial strain on the MoS<sub>2</sub> band gap

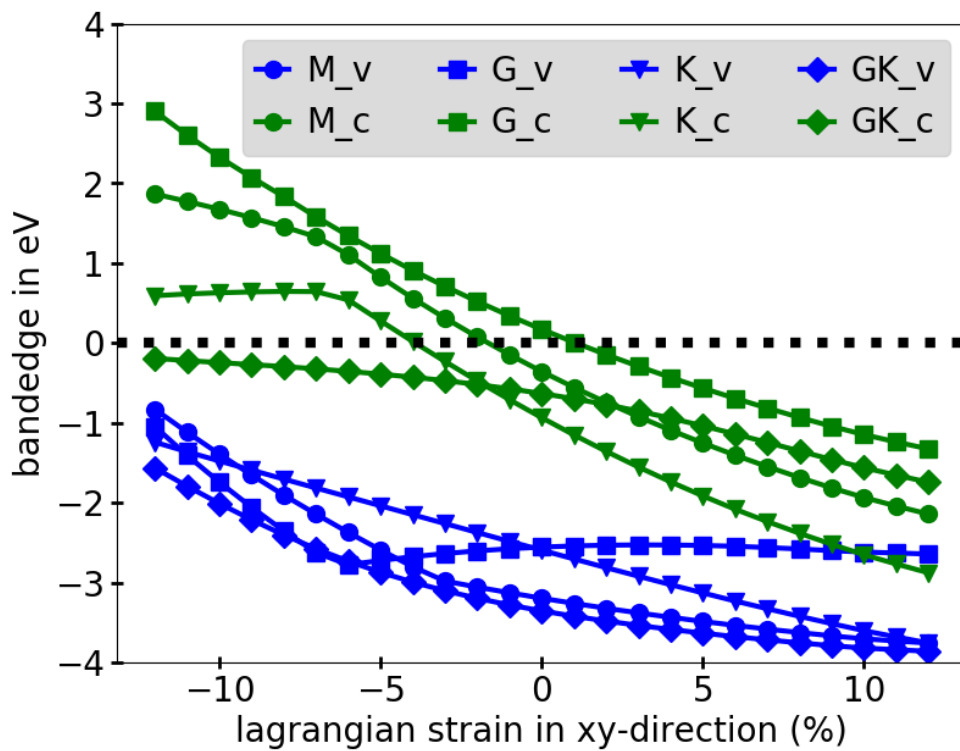


**Figure 6.1:** Band edges at the K-point of MoS<sub>2</sub> under biaxial strain.

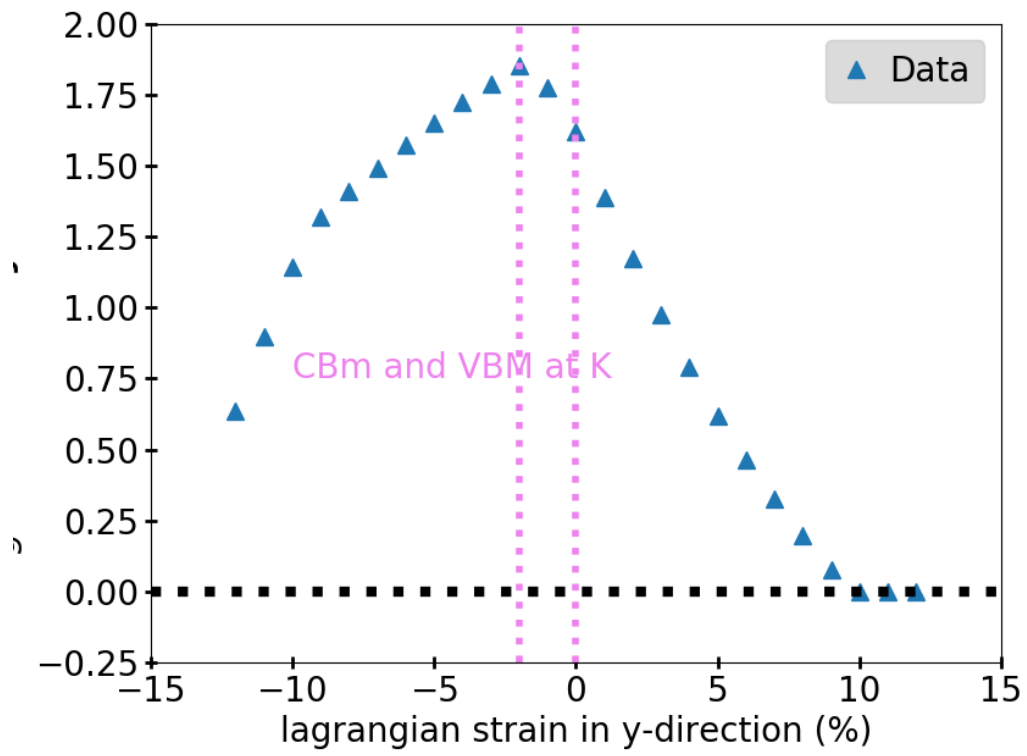


**Figure 6.2:** Band gap at the K-point of MoS<sub>2</sub>@Au(111) under biaxial strain.

---

## Appendix B: Species files

**Listing 1:** Species file for the element molybdenum.

```
1 <?xml version="1.0" encoding="UTF-8"?>
2 <spdb xsi:noNamespaceSchemaLocation="../../xml/species.xsd" xmlns:xsi="http://
  www.w3.org/2001/XMLSchema-instance">
3   <sp chemicalSymbol="Mo" name="molybdenum" z="-42.0000" mass="174887.9212">
4     <muffinTin rmin="0.100000E-06" radius="2.4000" rinf="25.8500"
      radialmeshPoints="1600"/>
5     <atomicState n="1" l="0" kappa="1" occ="2.00000" core="true"/>
6     <atomicState n="2" l="0" kappa="1" occ="2.00000" core="true"/>
7     <atomicState n="2" l="1" kappa="1" occ="2.00000" core="true"/>
8     <atomicState n="2" l="1" kappa="2" occ="4.00000" core="true"/>
9     <atomicState n="3" l="0" kappa="1" occ="2.00000" core="true"/>
10    <atomicState n="3" l="1" kappa="1" occ="2.00000" core="true"/>
11    <atomicState n="3" l="1" kappa="2" occ="4.00000" core="true"/>
12    <atomicState n="3" l="2" kappa="2" occ="4.00000" core="true"/>
13    <atomicState n="3" l="2" kappa="3" occ="6.00000" core="true"/>
14    <atomicState n="4" l="0" kappa="1" occ="2.00000" core="false"/>
15    <atomicState n="4" l="1" kappa="1" occ="2.00000" core="false"/>
16    <atomicState n="4" l="1" kappa="2" occ="4.00000" core="false"/>
17    <atomicState n="4" l="2" kappa="2" occ="3.00000" core="false"/>
18    <atomicState n="4" l="2" kappa="3" occ="2.00000" core="false"/>
19    <atomicState n="5" l="0" kappa="1" occ="1.00000" core="false"/>
20    <basis>
21      <default type="lapw" trialEnergy="0.1500" searchE="false"/>
22
23      <custom l="0" type="lapw" trialEnergy="3.7385" searchE="false"/>
24      <lo l="0">
25        <wf matchingOrder="0" trialEnergy="3.7385" searchE="false"/>
26        <wf matchingOrder="1" trialEnergy="3.7385" searchE="false"/>
27      </lo>
28      <lo l="0">
29        <wf matchingOrder="0" trialEnergy="3.7385" searchE="false"/>
30        <wf matchingOrder="2" trialEnergy="3.7385" searchE="false"/>
31      </lo>
32      <lo l="0">
33        <wf matchingOrder="0" trialEnergy="3.7385" searchE="false"/>
34        <wf matchingOrder="3" trialEnergy="3.7385" searchE="false"/>
35      </lo>
36      <lo l="0">
```

```

37     <wf matchingOrder="0" trialEnergy="3.7385" searchE="false" />
38     <wf matchingOrder="0" trialEnergy="-2.3039" searchE="false" />
39 </lo>
40 <lo l="0">
41     <wf matchingOrder="0" trialEnergy="-2.3039" searchE="false" />
42     <wf matchingOrder="1" trialEnergy="-2.3039" searchE="false" />
43 </lo>
44
45 <custom l="1" type="lapw" trialEnergy="-1.2677" searchE="false" />
46 <lo l="1">
47     <wf matchingOrder="0" trialEnergy="-1.2677" searchE="false" />
48     <wf matchingOrder="1" trialEnergy="-1.2677" searchE="false" />
49 </lo>
50 <lo l="1">
51     <wf matchingOrder="0" trialEnergy="-1.2677" searchE="false" />
52     <wf matchingOrder="2" trialEnergy="-1.2677" searchE="false" />
53 </lo>
54 <lo l="1">
55     <wf matchingOrder="0" trialEnergy="-1.2677" searchE="false" />
56     <wf matchingOrder="3" trialEnergy="-1.2677" searchE="false" />
57 </lo>
58
59 <custom l="2" type="lapw" trialEnergy="0.3972" searchE="false" />
60 <lo l="2">
61     <wf matchingOrder="0" trialEnergy="0.3972" searchE="false" />
62     <wf matchingOrder="1" trialEnergy="0.3972" searchE="false" />
63 </lo>
64 <lo l="2">
65     <wf matchingOrder="0" trialEnergy="0.3972" searchE="false" />
66     <wf matchingOrder="2" trialEnergy="0.3972" searchE="false" />
67 </lo>
68 <lo l="2">
69     <wf matchingOrder="0" trialEnergy="0.3972" searchE="false" />
70     <wf matchingOrder="3" trialEnergy="0.3972" searchE="false" />
71 </lo>
72
73 <custom l="3" type="lapw" trialEnergy="0.1500" searchE="false" />
74 <lo l="3">
75     <wf matchingOrder="0" trialEnergy="0.1500" searchE="false" />
76     <wf matchingOrder="1" trialEnergy="0.1500" searchE="false" />
77 </lo>
78 <lo l="3">
79     <wf matchingOrder="0" trialEnergy="0.1500" searchE="false" />
80     <wf matchingOrder="0" trialEnergy="4.2431" searchE="false" />
81 </lo>
82 <lo l="3">
83     <wf matchingOrder="0" trialEnergy="0.1500" searchE="false" />
84     <wf matchingOrder="0" trialEnergy="8.9657" searchE="false" />
85 </lo>
86
87 <custom l="4" type="lapw" trialEnergy="0.1500" searchE="false" />
88 <lo l="4">
89     <wf matchingOrder="0" trialEnergy="0.1500" searchE="false" />
90     <wf matchingOrder="1" trialEnergy="0.1500" searchE="false" />
91 </lo>

```

```
92 <lo l="4">
93   <wf matchingOrder="0" trialEnergy="0.1500" searchE="false" />
94   <wf matchingOrder="0" trialEnergy="7.5658" searchE="false" />
95 </lo>
96
97 <custom l="5" type="lapw" trialEnergy="0.1500" searchE="false" />
98 <lo l="5">
99   <wf matchingOrder="0" trialEnergy="0.1500" searchE="false" />
100   <wf matchingOrder="1" trialEnergy="0.1500" searchE="false" />
101 </lo>
102
103 <custom l="6" type="lapw" trialEnergy="0.1500" searchE="false" />
104 <lo l="6">
105   <wf matchingOrder="0" trialEnergy="0.1500" searchE="false" />
106   <wf matchingOrder="1" trialEnergy="0.1500" searchE="false" />
107 </lo>
108 </basis>
109
110 </sp>
111 </spdb>
```

## Listing 2: Species file for the element sulfur.

```
1 <?xml version="1.0" encoding="UTF-8"?>
2 <spdb xsi:noNamespaceSchemaLocation="../../xml/species.xsd" xmlns:xsi="http://
  www.w3.org/2001/XMLSchema-instance">
3 <sp chemicalSymbol="S" name="sulphur" z="-16.0000" mass="58452.74216">
4 <muffinTin rmin="0.100000E-05" radius="2.0500" rinf="20.3453"
  radialmeshPoints="1000"/>
5 <atomicState n="1" l="0" kappa="1" occ="2.00000" core="true"/>
6 <atomicState n="2" l="0" kappa="1" occ="2.00000" core="true"/>
7 <atomicState n="2" l="1" kappa="1" occ="2.00000" core="false"/>
8 <atomicState n="2" l="1" kappa="2" occ="4.00000" core="false"/>
9 <atomicState n="3" l="0" kappa="1" occ="2.00000" core="false"/>
10 <atomicState n="3" l="1" kappa="1" occ="2.00000" core="false"/>
11 <atomicState n="3" l="1" kappa="2" occ="2.00000" core="false"/>
12 <basis>
13 <default type="lapw" trialEnergy="0.1500" searchE="false"/>
14
15 <custom l="0" type="lapw" trialEnergy="0.0144" searchE="false"/>
16 <lo l="0">
17 <wf matchingOrder="0" trialEnergy="0.0144" searchE="false"/>
18 <wf matchingOrder="1" trialEnergy="0.0144" searchE="false"/>
19 </lo>
20 <lo l="0">
21 <wf matchingOrder="0" trialEnergy="0.0144" searchE="false"/>
22 <wf matchingOrder="2" trialEnergy="0.0144" searchE="false"/>
23 </lo>
24
25 <custom l="1" type="lapw" trialEnergy="0.5771" searchE="false"/>
26 <lo l="1">
27 <wf matchingOrder="0" trialEnergy="0.5771" searchE="false"/>
28 <wf matchingOrder="1" trialEnergy="0.5771" searchE="false"/>
29 </lo>
30 <lo l="1">
31 <wf matchingOrder="0" trialEnergy="0.5771" searchE="false"/>
32 <wf matchingOrder="2" trialEnergy="0.5771" searchE="false"/>
33 </lo>
34 <lo l="1">
35 <wf matchingOrder="0" trialEnergy="0.5771" searchE="false"/>
36 <wf matchingOrder="0" trialEnergy="-5.6330" searchE="false"/>
37 </lo>
38 <lo l="1">
39 <wf matchingOrder="0" trialEnergy="-5.6330" searchE="false"/>
40 <wf matchingOrder="1" trialEnergy="-5.6330" searchE="false"/>
41 </lo>
42
43 <custom l="2" type="lapw" trialEnergy="0.1500" searchE="false"/>
44 <lo l="2">
45 <wf matchingOrder="0" trialEnergy="0.1500" searchE="false"/>
46 <wf matchingOrder="1" trialEnergy="0.1500" searchE="false"/>
47 </lo>
48 <lo l="2">
49 <wf matchingOrder="0" trialEnergy="0.1500" searchE="false"/>
50 <wf matchingOrder="0" trialEnergy="4.6338" searchE="false"/>
51 </lo>
52
```

```

53 <custom l="3" type="lapw" trialEnergy="0.1500" searchE="false" />
54 <lo l="3">
55   <wf matchingOrder="0" trialEnergy="0.1500" searchE="false" />
56   <wf matchingOrder="1" trialEnergy="0.1500" searchE="false" />
57 </lo>
58 <lo l="3">
59   <wf matchingOrder="0" trialEnergy="0.1500" searchE="false" />
60   <wf matchingOrder="0" trialEnergy="8.3862" searchE="false" />
61 </lo>
62
63 <custom l="4" type="lapw" trialEnergy="0.1500" searchE="false" />
64 <lo l="4">
65   <wf matchingOrder="0" trialEnergy="0.1500" searchE="false" />
66   <wf matchingOrder="1" trialEnergy="0.1500" searchE="false" />
67 </lo>
68
69 <custom l="5" type="lapw" trialEnergy="0.1500" searchE="false" />
70 <lo l="5">
71   <wf matchingOrder="0" trialEnergy="0.1500" searchE="false" />
72   <wf matchingOrder="1" trialEnergy="0.1500" searchE="false" />
73 </lo>
74
75 <custom l="6" type="lapw" trialEnergy="0.1500" searchE="false" />
76 <lo l="6">
77   <wf matchingOrder="0" trialEnergy="0.1500" searchE="false" />
78   <wf matchingOrder="1" trialEnergy="0.1500" searchE="false" />
79 </lo>
80 </basis>
81
82 </sp>
83 </spdb>

```

### Listing 3: Species file for the element gold.

```
1 <?xml version="1.0" encoding="UTF-8"?>
2 <spdb xsi:noNamespaceSchemaLocation="../../xml/species.xsd" xmlns:xsi="http://
  www.w3.org/2001/XMLSchema-instance">
3   <sp chemicalSymbol="Au" name="gold" z="-79.0000" mass="359048.0559">
4     <muffinTin rmin="0.100000E-04" radius="2.6000" rinf="21.6740"
      radialmeshPoints="900"/>
5     <atomicState n="1" l="0" kappa="1" occ="2.00000" core="true"/>
6     <atomicState n="2" l="0" kappa="1" occ="2.00000" core="true"/>
7     <atomicState n="2" l="1" kappa="1" occ="2.00000" core="true"/>
8     <atomicState n="2" l="1" kappa="2" occ="4.00000" core="true"/>
9     <atomicState n="3" l="0" kappa="1" occ="2.00000" core="true"/>
10    <atomicState n="3" l="1" kappa="1" occ="2.00000" core="true"/>
11    <atomicState n="3" l="1" kappa="2" occ="4.00000" core="true"/>
12    <atomicState n="3" l="2" kappa="2" occ="4.00000" core="true"/>
13    <atomicState n="3" l="2" kappa="3" occ="6.00000" core="true"/>
14    <atomicState n="4" l="0" kappa="1" occ="2.00000" core="true"/>
15    <atomicState n="4" l="1" kappa="1" occ="2.00000" core="true"/>
16    <atomicState n="4" l="1" kappa="2" occ="4.00000" core="true"/>
17    <atomicState n="4" l="2" kappa="2" occ="4.00000" core="true"/>
18    <atomicState n="4" l="2" kappa="3" occ="6.00000" core="true"/>
19    <atomicState n="5" l="0" kappa="1" occ="2.00000" core="true"/>
20    <atomicState n="4" l="3" kappa="3" occ="6.00000" core="false"/>
21    <atomicState n="4" l="3" kappa="4" occ="8.00000" core="false"/>
22    <atomicState n="5" l="1" kappa="1" occ="2.00000" core="false"/>
23    <atomicState n="5" l="1" kappa="2" occ="4.00000" core="false"/>
24    <atomicState n="5" l="2" kappa="2" occ="4.00000" core="false"/>
25    <atomicState n="5" l="2" kappa="3" occ="6.00000" core="false"/>
26    <atomicState n="6" l="0" kappa="1" occ="1.00000" core="false"/>
27    <basis>
28      <default type="lapw" trialEnergy="0.1500" searchE="false"/>
29
30      <custom l="0" type="lapw" trialEnergy="0.1500" searchE="false"/>
31      <lo l="0">
32        <wf matchingOrder="0" trialEnergy="0.1500" searchE="false"/>
33        <wf matchingOrder="1" trialEnergy="0.1500" searchE="false"/>
34      </lo>
35      <lo l="0">
36        <wf matchingOrder="0" trialEnergy="0.1500" searchE="false"/>
37        <wf matchingOrder="0" trialEnergy="2.2000" searchE="false"/>
38      </lo>
39      <lo l="0">
40        <wf matchingOrder="0" trialEnergy="2.2000" searchE="false"/>
41        <wf matchingOrder="1" trialEnergy="2.2000" searchE="false"/>
42      </lo>
43
44      <custom l="1" type="lapw" trialEnergy="0.1500" searchE="false"/>
45      <lo l="1">
46        <wf matchingOrder="0" trialEnergy="0.1500" searchE="false"/>
47        <wf matchingOrder="1" trialEnergy="0.1500" searchE="false"/>
48      </lo>
49      <lo l="1">
50        <wf matchingOrder="0" trialEnergy="0.1500" searchE="false"/>
51        <wf matchingOrder="1" trialEnergy="-7.0000" searchE="false"/>
52      </lo>
```

```

53 <lo l="1">
54   <wf matchingOrder="0" trialEnergy="0.1500" searchE="false" />
55   <wf matchingOrder="0" trialEnergy="-0.3000" searchE="false" />
56 </lo>
57 <lo l="1">
58   <wf matchingOrder="0" trialEnergy="-0.3000" searchE="false" />
59   <wf matchingOrder="1" trialEnergy="-0.3000" searchE="false" />
60 </lo>
61 <lo l="1">
62   <wf matchingOrder="0" trialEnergy="-7.0000" searchE="false" />
63   <wf matchingOrder="1" trialEnergy="-7.0000" searchE="false" />
64 </lo>
65
66 <lo l="1">
67   <wf matchingOrder="0" trialEnergy="0.1500" searchE="false" />
68   <wf matchingOrder="0" trialEnergy="5.3033" searchE="false" />
69 </lo>
70
71 <custom l="2" type="lapw" trialEnergy="0.1500" searchE="false" />
72 <lo l="2">
73   <wf matchingOrder="0" trialEnergy="0.1500" searchE="false" />
74   <wf matchingOrder="1" trialEnergy="0.1500" searchE="false" />
75 </lo>
76 <lo l="2">
77   <wf matchingOrder="0" trialEnergy="0.1500" searchE="false" />
78   <wf matchingOrder="0" trialEnergy="-4.7000" searchE="false" />
79 </lo>
80 <lo l="2">
81   <wf matchingOrder="0" trialEnergy="-4.7000" searchE="false" />
82   <wf matchingOrder="1" trialEnergy="-4.7000" searchE="false" />
83 </lo>
84 <lo l="2">
85   <wf matchingOrder="0" trialEnergy="0.1500" searchE="false" />
86   <wf matchingOrder="0" trialEnergy="0.8000" searchE="false" />
87 </lo>
88 <lo l="2">
89   <wf matchingOrder="0" trialEnergy="0.8000" searchE="false" />
90   <wf matchingOrder="1" trialEnergy="0.8000" searchE="false" />
91 </lo>
92
93 <lo l="2">
94   <wf matchingOrder="0" trialEnergy="0.1500" searchE="false" />
95   <wf matchingOrder="0" trialEnergy="6.9332" searchE="false" />
96 </lo>
97
98 <custom l="3" type="lapw" trialEnergy="0.1500" searchE="false" />
99 <lo l="3">
100   <wf matchingOrder="0" trialEnergy="0.1500" searchE="false" />
101   <wf matchingOrder="1" trialEnergy="0.1500" searchE="false" />
102 </lo>
103 <lo l="3">
104   <wf matchingOrder="0" trialEnergy="0.1500" searchE="false" />
105   <wf matchingOrder="0" trialEnergy="-3.0000" searchE="false" />
106 </lo>
107 <lo l="3">

```

```

108     <wf matchingOrder="0" trialEnergy="-3.0000" searchE="false" />
109     <wf matchingOrder="1" trialEnergy="-3.0000" searchE="false" />
110 </lo>
111 <lo l="3">
112     <wf matchingOrder="0" trialEnergy="0.1500" searchE="false" />
113     <wf matchingOrder="0" trialEnergy="4.3522" searchE="false" />
114 </lo>
115 <lo l="3">
116     <wf matchingOrder="0" trialEnergy="0.1500" searchE="false" />
117     <wf matchingOrder="0" trialEnergy="9.0495" searchE="false" />
118 </lo>
119
120 <custom l="4" type="lapw" trialEnergy="0.1500" searchE="false" />
121 <lo l="4">
122     <wf matchingOrder="0" trialEnergy="0.1500" searchE="false" />
123     <wf matchingOrder="1" trialEnergy="0.1500" searchE="false" />
124 </lo>
125 <lo l="4">
126     <wf matchingOrder="0" trialEnergy="0.1500" searchE="false" />
127     <wf matchingOrder="0" trialEnergy="6.1917" searchE="false" />
128 </lo>
129
130 <custom l="5" type="lapw" trialEnergy="0.1500" searchE="false" />
131 <lo l="5">
132     <wf matchingOrder="0" trialEnergy="0.1500" searchE="false" />
133     <wf matchingOrder="1" trialEnergy="0.1500" searchE="false" />
134 </lo>
135 <lo l="5">
136     <wf matchingOrder="0" trialEnergy="0.1500" searchE="false" />
137     <wf matchingOrder="0" trialEnergy="8.9719" searchE="false" />
138 </lo>
139
140 <custom l="6" type="lapw" trialEnergy="0.1500" searchE="false" />
141 <lo l="6">
142     <wf matchingOrder="0" trialEnergy="0.1500" searchE="false" />
143     <wf matchingOrder="1" trialEnergy="0.1500" searchE="false" />
144 </lo>
145 </basis>
146
147 </sp>
148 </spdb>

```

---

## References

- [1] NOVOSELOV, K. S. ; GEIM, A. K. ; MOROZOV, S. V. ; JIANG, D. ; ZHANG, Y. ; DUBONOS, S. V. ; GRIGORIEVA, I. V. ; FIRSOV, A. A.: Electric Field Effect in Atomically Thin Carbon Films. In: *Science* 306 (2004), oct, Nr. 5696, S. 666–669. <http://dx.doi.org/10.1126/science.1102896>. – DOI 10.1126/science.1102896
- [2] GEIM, A. K. ; GRIGORIEVA, I. V.: Van der Waals heterostructures. In: *Nature* 499 (2013), jul, Nr. 7459, S. 419–425. <http://dx.doi.org/10.1038/nature12385>. – DOI 10.1038/nature12385
- [3] NOURBAKHS, Amirhasan ; ZUBAIR, Ahmad ; SAJJAD, Redwan N. ; G., Amir Tavakkoli K. ; CHEN, Wei ; FANG, Shiang ; LING, Xi ; KONG, Jing ; DRESSELHAUS, Mildred S. ; KAXIRAS, Efthimios ; BERGGREN, Karl K. ; ANTONIADIS, Dimitri ; PALACIOS, Tomás: MoS<sub>2</sub> Field-Effect Transistor with Sub-10 nm Channel Length. In: *Nano Letters* 16 (2016), nov, Nr. 12, S. 7798–7806. <http://dx.doi.org/10.1021/acs.nanolett.6b03999>. – DOI 10.1021/acs.nanolett.6b03999
- [4] RADISAVLJEVIC, B. ; RADENOVIC, A. ; BRIVIO, J. ; GIACOMETTI, V. ; KIS, A.: Single-layer MoS<sub>2</sub> transistors. In: *Nature Nanotechnology* 6 (2011), jan, Nr. 3, S. 147–150. <http://dx.doi.org/10.1038/nnano.2010.279>. – DOI 10.1038/nnano.2010.279
- [5] BERNARDI, Marco ; PALUMMO, Maurizia ; GROSSMAN, Jeffrey C.: Extraordinary Sunlight Absorption and One Nanometer Thick Photovoltaics Using Two-Dimensional Monolayer Materials. In: *Nano Letters* 13 (2013), jul, Nr. 8, S. 3664–3670. <http://dx.doi.org/10.1021/nl401544y>. – DOI 10.1021/nl401544y
- [6] COLEMAN, Jonathan N. ; LOTYA, Mustafa ; O'NEILL, Arlene ; BERGIN, Shane D. ; KING, Paul J. ; KHAN, Umar ; YOUNG, Karen ; GAUCHER, Alexandre ; DE, Sukanta ; SMITH, Ronan J. ; SHVETS, Igor V. ; ARORA, Sunil K. ; STANTON, George ; KIM, Hye-Young ; LEE, Kangho ; KIM, Gyu T.

- ; DUESBERG, Georg S. ; HALLAM, Toby ; BOLAND, John J. ; WANG, Jing J. ; DONEGAN, John F. ; GRUNLAN, Jaime C. ; MORIARTY, Gregory ; SHMELIOV, Aleksey ; NICHOLLS, Rebecca J. ; PERKINS, James M. ; GRIEVESON, Eleanor M. ; THEUWISSEN, Koenraad ; MCCOMB, David W. ; NELLIST, Peter D. ; NICOLOSI, Valeria: Two-Dimensional Nanosheets Produced by Liquid Exfoliation of Layered Materials. In: Science 331 (2011), feb, Nr. 6017, S. 568–571. <http://dx.doi.org/10.1126/science.1194975>. – DOI 10.1126/science.1194975
- [7] LEE, Yi-Hsien ; ZHANG, Xin-Quan ; ZHANG, Wenjing ; CHANG, Mu-Tung ; LIN, Cheng-Te ; CHANG, Kai-Di ; YU, Ya-Chu ; WANG, Jacob Tse-Wei ; CHANG, Chia-Seng ; LI, Lain-Jong ; LIN, Tsung-Wu: Synthesis of Large-Area MoS<sub>2</sub> Atomic Layers with Chemical Vapor Deposition. In: Advanced Materials 24 (2012), mar, Nr. 17, S. 2320–2325. <http://dx.doi.org/10.1002/adma.201104798>. – DOI 10.1002/adma.201104798
- [8] WANG, Qing H. ; KALANTAR-ZADEH, Kouros ; KIS, Andras ; COLEMAN, Jonathan N. ; STRANO, Michael S.: Electronics and optoelectronics of two-dimensional transition metal dichalcogenides. In: Nature Nanotechnology 7 (2012), nov, Nr. 11, S. 699–712. <http://dx.doi.org/10.1038/nnano.2012.193>. – DOI 10.1038/nnano.2012.193
- [9] MAK, Kin F. ; LEE, Changgu ; HONE, James ; SHAN, Jie ; HEINZ, Tony F.: Atomically Thin MoS<sub>2</sub>: A New Direct-Gap Semiconductor. In: Physical Review Letters 105 (2010), sep, Nr. 13, S. 136805. <http://dx.doi.org/10.1103/physrevlett.105.136805>. – DOI 10.1103/physrevlett.105.136805
- [10] KRANE, Nils ; LOTZE, Christian ; FRANKE, Katharina J.: Moiré structure of MoS<sub>2</sub> on Au(111): Local structural and electronic properties. In: Surface Science 678 (2018), dec, S. 136–142. <http://dx.doi.org/10.1016/j.susc.2018.03.015>. – DOI 10.1016/j.susc.2018.03.015
- [11] GULANS, Andris ; KONTUR, Stefan ; MEISENBICHLER, Christian ; NABOK, Dmitrii ; PAVONE, Pasquale ; RIGAMONTI, Santiago ; SAGMEISTER, Stephan ; WERNER, Ute ; DRAXL, Claudia: exciting: a full-potential all-electron package implementing density-functional theory and many-body perturbation theory. In: Journal of Physics: Condensed Matter 26 (2014), aug, Nr. 36, S. 363202. <http://dx.doi.org/10.1088/0953-8984/26/36/363202>. – DOI 10.1088/0953-8984/26/36/363202
- [12] BORN, M. ; OPPENHEIMER, R.: Zur Quantentheorie der Molekeln. In: Annalen der Physik 389 (1927), Nr. 20, S. 457–484. <http://dx.doi.org/10.1002/andp.19273892002>. – DOI 10.1002/andp.19273892002
- [13] HOHENBERG, P. ; KOHN, W.: Inhomogeneous Electron Gas. In: Physical Review 136 (1964), nov, Nr. 3B, S. B864–B871. <http://dx.doi.org/10.1103/physrev.136.b864>. – DOI 10.1103/physrev.136.b864

- [14] KOHN, W. ; SHAM, L. J.: Self-Consistent Equations Including Exchange and Correlation Effects. In: Physical Review 140 (1965), nov, Nr. 4A, S. A1133–A1138. <http://dx.doi.org/10.1103/physrev.140.a1133>. – DOI 10.1103/physrev.140.a1133
- [15] WEBER, Peter: Elastic and lattice-dynamical properties of titanium-based compounds, Humboldt-Universität zu Berlin, Diplomarbeit, 2019
- [16] PERDEW, John P. ; ERNZERHOF, Matthias ; BURKE, Kieron: Rationale for mixing exact exchange with density functional approximations. In: The Journal of Chemical Physics 105 (1996), dec, Nr. 22, S. 9982–9985. <http://dx.doi.org/10.1063/1.472933>. – DOI 10.1063/1.472933
- [17] PERDEW, John P. ; BURKE, Kieron ; ERNZERHOF, Matthias: Generalized Gradient Approximation Made Simple. In: Physical Review Letters 77 (1996), oct, Nr. 18, S. 3865–3868. <http://dx.doi.org/10.1103/physrevlett.77.3865>. – DOI 10.1103/physrevlett.77.3865
- [18] PERDEW, John P.: Jacob's ladder of density functional approximations for the exchange-correlation energy. In: AIP Conference Proceedings, AIP, 2001
- [19] PERDEW, John P. ; BURKE, Kieron ; ERNZERHOF, Matthias: Generalized Gradient Approximation Made Simple. In: Phys. Rev. Lett. 77 (1996), Oct, 3865–3868. <http://dx.doi.org/10.1103/PhysRevLett.77.3865>. – DOI 10.1103/PhysRevLett.77.3865
- [20] MUELLER, Thomas ; MALIC, Ermin: Exciton physics and device application of two-dimensional transition metal dichalcogenide semiconductors. In: npj 2D Materials and Applications 2 (2018), sep, Nr. 1. <http://dx.doi.org/10.1038/s41699-018-0074-2>. – DOI 10.1038/s41699-018-0074-2
- [21] HEDIN, Lars: New Method for Calculating the One-Particle Green's Function with Application to the Electron-Gas Problem. In: Physical Review 139 (1965), aug, Nr. 3A, S. A796–A823. <http://dx.doi.org/10.1103/physrev.139.a796>. – DOI 10.1103/physrev.139.a796
- [22] HYBERTSEN, Mark S. ; LOUIE, Steven G.: Electron correlation in semiconductors and insulators: Band gaps and quasiparticle energies. In: Physical Review B 34 (1986), oct, Nr. 8, S. 5390–5413. <http://dx.doi.org/10.1103/physrevb.34.5390>. – DOI 10.1103/physrevb.34.5390
- [23] SALPETER, E. E. ; BETHE, H. A.: A Relativistic Equation for Bound-State Problems. In: Physical Review 84 (1951), dec, Nr. 6, S. 1232–1242. <http://dx.doi.org/10.1103/physrev.84.1232>. – DOI 10.1103/physrev.84.1232
- [24] MARTIN, Richard M. ; REINING, Lucia ; CEPERLEY, David M.: Interacting Electrons: Theory and Computational Approaches. Cambridge

University Press, 2016. <http://dx.doi.org/10.1017/CB09781139050807>.  
<http://dx.doi.org/10.1017/CB09781139050807>

- [25] SAGMEISTER, Stephan ; AMBROSCH-DRAXL, Claudia: Time-dependent density functional theory versus Bethe–Salpeter equation: an all-electron study. In: *Physical Chemistry Chemical Physics* 11 (2009), Nr. 22, S. 4451. <http://dx.doi.org/10.1039/b903676h>. – DOI 10.1039/b903676h
- [26] SANDER, Tobias ; MAGGIO, Emanuele ; KRESSE, Georg: Beyond the Tamm-Dancoff approximation for extended systems using exact diagonalization. In: *Physical Review B* 92 (2015), jul, Nr. 4, S. 045209. <http://dx.doi.org/10.1103/physrevb.92.045209>. – DOI 10.1103/physrevb.92.045209
- [27] SJÖSTEDT, E ; NORDSTRÖM, L ; SINGH, D.J: An alternative way of linearizing the augmented plane-wave method. In: *Solid State Communications* 114 (2000), mar, Nr. 1, S. 15–20. [http://dx.doi.org/10.1016/s0038-1098\(99\)00577-3](http://dx.doi.org/10.1016/s0038-1098(99)00577-3). – DOI 10.1016/s0038-1098(99)00577-3
- [28] KIM, Jongmin ; GULANS, Andris ; DRAXL, Claudia: Robust mixing in self-consistent linearized augmented planewave calculations. In: *Electronic Structure* 2 (2020), aug, Nr. 3, S. 037001. <http://dx.doi.org/10.1088/2516-1075/ababde>. – DOI 10.1088/2516-1075/ababde
- [29] NABOK, Dmitrii ; GULANS, Andris ; DRAXL, Claudia: Accurate all-electron  $G_0W_0$  quasiparticle energies employing the full-potential augmented plane-wave method. In: *Physical Review B* 94 (2016), jul, Nr. 3, S. 035118. <http://dx.doi.org/10.1103/physrevb.94.035118>. – DOI 10.1103/physrevb.94.035118
- [30] GLANTSCHNIG, Kathrin: *First principles calculation of optical spectra*, Universitätsbibliothek Graz, Diss., 2014
- [31] YOUNG, P A.: Lattice parameter measurements on molybdenum disulphide. In: *Journal of Physics D: Applied Physics* 1 (1968), jul, Nr. 7, S. 936–938. <http://dx.doi.org/10.1088/0022-3727/1/7/416>. – DOI 10.1088/0022-3727/1/7/416
- [32] JETTE, Eric R. ; FOOTE, Frank: Precision Determination of Lattice Constants. In: *The Journal of Chemical Physics* 3 (1935), oct, Nr. 10, S. 605–616. <http://dx.doi.org/10.1063/1.1749562>. – DOI 10.1063/1.1749562
- [33] LAZIĆ, Predrag: CellMatch: Combining two unit cells into a common supercell with minimal strain. In: *Computer Physics Communications* 197 (2015), 324–334. <http://dx.doi.org/https://doi.org/10.1016/j.cpc.2015.08.038>. – DOI <https://doi.org/10.1016/j.cpc.2015.08.038>. – ISSN 0010-4655
- [34] BRUIX, Albert ; MIWA, Jill A. ; HAUPTMANN, Nadine ; WEGNER, Daniel ; ULSTRUP, Søren ; GRØNBORG, Signe S. ; SANDERS, Charlotte E.

- ; DENDZIK, Maciej ; GRUBI, Antonija ; BIANCHI, Marco ; LAURITSEN, Jeppe V. ; KHAJETOORIANS, Alexander A. ; HAMMER, Bjørk ; HOFMANN, Philip: Single-layer MoS<sub>2</sub> on Au(111): Band gap renormalization and substrate interaction. In: *Phys. Rev. B* 93 (2016), Apr, 165422. <http://dx.doi.org/10.1103/PhysRevB.93.165422>. – DOI 10.1103/PhysRevB.93.165422
- [35] TABATABAEI, Seyed M. ; NOEI, Maziar ; KHALIJI, Kaveh ; POURFATH, Mahdi ; FATHIPOUR, Morteza: A first-principles study on the effect of biaxial strain on the ultimate performance of monolayer MoS<sub>2</sub>-based double gate field effect transistor. In: *Journal of Applied Physics* 113 (2013), apr, Nr. 16, S. 163708. <http://dx.doi.org/10.1063/1.4803032>. – DOI 10.1063/1.4803032
- [36] RYOU, Junga ; KIM, Yong-Sung ; KC, Santosh ; CHO, Kyeongjae: Monolayer MoS<sub>2</sub> Bandgap Modulation by Dielectric Environments and Tunable Bandgap Transistors. In: *Scientific Reports* 6 (2016), jul, Nr. 1. <http://dx.doi.org/10.1038/srep29184>. – DOI 10.1038/srep29184
- [37] BAHMANI, Mohammad ; FAGHIHNASIRI, Mahdi ; LORKE, Michael ; KUC, Agnieszka-Beata ; FRAUENHEIM, Thomas: Electronic Properties of Defective MoS<sub>2</sub> Monolayers Subject to Mechanical Deformations: A First-Principles Approach. In: *physica status solidi (b)* 257 (2020), mar, Nr. 5, S. 1900541. <http://dx.doi.org/10.1002/pssb.201900541>. – DOI 10.1002/pssb.201900541
- [38] ROLDÁN, Rafael ; SILVA-GUILLÉN, Jose A. ; LÓPEZ-SANCHO, M. P. ; GUINEA, Francisco ; CAPPELLUTI, Emmanuele ; ORDEJÓN, Pablo: Electronic properties of single-layer and multilayer transition metal dichalcogenides MX<sub>2</sub> (M = Mo, W and X= S, Se). In: *Annalen der Physik* 526 (2014), sep, Nr. 9-10, S. 347–357. <http://dx.doi.org/10.1002/andp.201400128>. – DOI 10.1002/andp.201400128
- [39] GONG, Cheng ; COLOMBO, Luigi ; WALLACE, Robert M. ; CHO, Kyeongjae: The Unusual Mechanism of Partial Fermi Level Pinning at Metal–MoS<sub>2</sub> Interfaces. In: *Nano Letters* 14 (2014), mar, Nr. 4, S. 1714–1720. <http://dx.doi.org/10.1021/nl403465v>. – DOI 10.1021/nl403465v
- [40] SHI, Hongliang ; PAN, Hui ; ZHANG, Yong-Wei ; YAKOBSON, Boris I.: Quasiparticle band structures and optical properties of strained monolayer MoS. In: *Physical Review B* 87 (2013), apr, Nr. 15, S. 155304. <http://dx.doi.org/10.1103/physrevb.87.155304>. – DOI 10.1103/physrevb.87.155304
- [41] KOMSA, Hannu-Pekka ; KRASHENINNIKOV, Arkady V.: Effects of confinement and environment on the electronic structure and exciton binding energy of MoS. In: *Physical Review B* 86 (2012), dec, Nr. 24, S. 241201. <http://dx.doi.org/10.1103/physrevb.86.241201>. – DOI 10.1103/phys-

- [42] PARK, Soohyung ; MUTZ, Niklas ; SCHULTZ, Thorsten ; BLUMSTENGEL, Sylke ; HAN, Ali ; ALJARB, Areej ; LI, Lain-Jong ; LIST-KRATOCHVIL, Emil J W. ; AMSALEM, Patrick ; KOCH, Norbert: Direct determination of monolayer MoS<sub>2</sub> exciton binding energies on insulating and metallic substrates. In: 2D Materials 5 (2018), jan, Nr. 2, S. 025003. <http://dx.doi.org/10.1088/2053-1583/aaa4ca>. – DOI 10.1088/2053-1583/aaa4ca
- [43] GUILHON, I. ; MARQUES, M. ; TELES, L. K. ; PALUMMO, M. ; PULCI, O. ; BOTTI, Silvana ; BECHSTEDT, F.: Out-of-plane excitons in two-dimensional crystals. In: Physical Review B 99 (2019), apr, Nr. 16, S. 161201. <http://dx.doi.org/10.1103/physrevb.99.161201>. – DOI 10.1103/physrevb.99.161201
- [44] EDALATI-BOOSTAN, Saeideh ; COCCHI, Caterina ; DRAXL, Claudia: MoTe<sub>2</sub> as a natural hyperbolic material across the visible and the ultraviolet region. In: Physical Review Materials 4 (2020), aug, Nr. 8, S. 085202. <http://dx.doi.org/10.1103/physrevmaterials.4.085202>. – DOI 10.1103/physrevmaterials.4.085202

---

# Selbständigkeitserklärung

Die vorliegende Masterarbeit wurde von mir unter Beachtung der im Jahr 2016 erlassenen Studienordnung für den Masterstudiengang Physik angefertigt. Hiermit versichere ich, dass ich diese wissenschaftliche Arbeit mit dem Titel „MoS<sub>2</sub> on gold substrate“ selbstständig verfasst und keine anderen als die angegebenen Quellen und Hilfsmittel verwendet habe sowie, dass ich hiermit erstmalig eine Masterarbeit im Studienfach Physik einreiche.

Berlin, der 21. September 2022